

1 **A global view of the stratospheric background, volcanic and**
2 **wildfire aerosol in the CALIOP era (2006 – 2023)**

3 Bengt G. Martinsson, Johan Friberg, and Moa K. Sporre

4 Department of Physics, Lund University, Lund, Sweden

5 *Correspondence to:* Bengt G. Martinsson (bengt.martinsson@fysik.lu.se)

6 **Abstract.** This study deals with the stratospheric aerosol during the 17 years of lidar
7 measurements with CALIOP aboard the CALIPSO satellite. To obtain extinction from the
8 backscattering measurements, we estimated the lidar ratios of the main aerosol
9 injections into the stratosphere. The stratospheric background is estimated by making a
10 subdivision of the stratosphere into nine parts, spanned by three latitude and altitude
11 intervals, reaching background conditions individually at different times. The extracted
12 background shows excellent agreement with SAGE II solar occultation measurements
13 in the volcanically quiescent period 1998 - 2000. Our results show that 70% of the
14 background aerosol in the deep Brewer-Dobson (dBD) branch is formed above 19 km
15 altitude, indicating strong influence of carbonyl sulfide on the stratospheric background
16 aerosol. The stratosphere was clearly affected by 15 volcanic eruptions and 5 wildfires.
17 Their combined aerosol load affected the Southern extratropics, tropics and Northern
18 extratropics almost equally, and the altitude distribution shows that the shallow Brewer-
19 Dobson branch was most affected (43%) followed by the dBD (31%) and lowermost
20 stratosphere (26%). The most important events in order of maximum AOD were the
21 Hunga Ha’apai eruption (2022), Australian wildfires (2019-20) and the eruptions of
22 Raikoke (2019), Sarychev (2009) and Nabro (2011). These events induced strong
23 variability in the yearly average global stratospheric aerosol optical depth (AOD), which
24 ranged from 0.0057 (background) to 0.016. CALIOP provided invaluable data for
25 stratospheric aerosol climatologies during its 17 years of operation.

26 **1. Introduction**

27 Tropospheric air, containing aerosol particles and the sulfurous aerosol precursor gases
28 carbonyl sulfide (OCS) and sulfur dioxide (SO₂), enter the stratosphere across the
29 tropical tropopause. These constituents form the stratospheric background aerosol
30 (Kremser et al., 2016), an aerosol layer that is located above 20 km altitude in the
31 tropics, and lower in the extratropics, containing water-soluble sulfur-rich particles
32 (Junge et al., 1961). Additional aerosol, that can be classified as background due to its
33 diffuse nature, originates from the Asian Tropopause Aerosol Layer (ATAL), an aerosol
34 layer between 13 – 18 km altitude over Asia (Vernier et al., 2015). The stratospheric
35 background aerosol contains sulfate, water, organics, and minor traces of tropospheric
36 aerosol and extraterrestrial material (Martinsson et al., 2005; Murphy et al., 2007;
37 Kremser et al., 2016; Martinsson et al., 2019).

38 The stratospheric aerosol load is highly variable due to special aerosol events
39 connected to volcanism (Bauman et al., 2003; Vernier et al., 2009; Solomon et al., 2011;
40 Andersson et al., 2015) and wildfires (Fromm et al., 2010; Martinsson et al., 2022;
41 Friberg et al., 2023, Peterson et al., 2025), which inject copious amounts of aerosol and
42 precursor gases affecting the stratospheric aerosol for months up to several years
43 (Friberg et al., 2018). These aerosol events induce a variability that needs to be
44 accounted for in climate models. From 1979, the satellite measurement era, the most
45 important volcanic eruptions, El Chichon in 1982 and Mt. Pinatubo (1991), caused a
46 maximum global 3-month average effective radiative forcing of -2 and -3 W/m²,
47 respectively (Schmidt et al., 2018). After a period of low volcanic influence on the
48 stratosphere around the turn of the millennium, many volcanic eruptions and wildfires
49 have affected the aerosol in the stratosphere. The most important are the 2019-20
50 Australian wildfires and the eruptions of Sarychev (2009), Raikoke (2019) and Hunga
51 Ha’apai (2022).

52 Fresh wildfire aerosol particles contain black carbon and a dominating fraction of
53 organics (Garofalo et al., 2019), where the latter is rapidly lost (half-life 10 days) in the
54 stratosphere due to photolysis (Martinsson et al., 2022). The composition of volcanic
55 stratospheric aerosol particles varies. SO₂-rich volcanic emissions, like the 2008

56 eruption of Kasatochi, are dominated by sulfate, some organics and a minor fraction of
57 ash (Martinsson et al., 2009, Andersson et al., 2013; Friberg et al., 2014). On the other
58 hand, SO₂-poor eruptions, like that of Puyehue-Cordón Caulle in 2011, are dominated
59 by ash (Clarisse et al., 2013). Steam-boosted eruptions of submarine volcanoes (Mastin
60 et al., 2024), like the 2022 eruption of Hunga Ha’apai, can result in a stratospheric
61 aerosol with a strong contribution from sea salt (Martinsson et al., 2025).

62 From the beginning of extensive satellite data in the late 1970s the stratospheric aerosol
63 load has usually been measured using solar occultation (Sato et al., 1993). GloSSAC
64 (Global Space-based Stratospheric Aerosol Climatology), a later construction of a
65 continuous record of optical properties of stratospheric aerosol spanning 1979 to
66 present, has a core of solar occultation measurement with the notable 22 year era of
67 SAGE II continuing a few years of solar occultation measurement by SAM II and SAGE I
68 (Thomason et al., 2018). Solar occultation became unavailable during 2005 – 2017. To
69 continue the GloSSAC record, other satellite-based measurements were deployed. The
70 limb scatter instrument OSIRIS (Rieger et al., 2015) and the lidar CALIOP (Cloud-Aerosol
71 Lidar with Orthogonal Polarization) (Winker et al., 2010) were, after substantial
72 recalibration (Thomason et al., 2018, Kovilakam et al., 2020, Kovilakam et al., 2023),
73 used to bridge the gap to obtain continuous time series of stratospheric aerosol
74 properties. Mixing data from many sources that are relying on different measurement
75 principles is however complex, as pointed out by Thomason et al. (2018). We will return
76 to this matter in the discussion section.

77 This work deals with the stratospheric aerosol in the CALIOP era, spanning the 17-year
78 period 2006-06-12 to 2023-06-30. CALIOP data (level 1B, version 4-51) is corrected for
79 attenuation, and the lidar ratio is estimated for the stratospheric aerosol resulting from
80 12 volcanic eruptions and wildfires. The stratosphere from the tropopause to 35 km
81 altitude is divided into three altitude and three latitude parts, in total nine parts, where
82 the backscattering of the background stratospheric aerosol is identified and its sources
83 discussed. By subtraction of the signal from the background aerosol, the backscattering
84 from major stratospheric aerosol events is obtained. This is converted to AOD using the
85 estimated lidar ratios. We find that global average aerosol backscattering intensity
86 exceeded the background by 55% in the 17 years studied. The strongest influence from

87 volcanism and wildfires was in 2022 and 2023 due to the submarine Hunga Ha’apai
88 eruption. The second strongest occurred in 2020 due to the Australian wildfires,
89 followed by 2009 (Sarychev eruption) and 2019 (mainly the Raikoke eruption). 2013 was
90 a year when the entire stratosphere was close to background conditions. Finally, we
91 discuss the validity of lidar data in comparison with the more established data based on
92 solar occultation.

93 **2. Methods**

94 This paper is based on measurements with the CALIOP lidar instrument aboard the
95 CALIPSO (Cloud-Aerosol Lidar and Infrared Pathfinder Satellite Observation) satellite
96 that completed approximately 15 orbits between latitudes -82 and 82° each day.

97 ***2.1 CALIOP properties and methods applied***

98 CALIOP with a laser of 532 nm wavelength produced vertical profiles of backscattering
99 intensity from air molecules, aerosol particles and cloud drops from the ground up to 35
100 km altitude with high vertical resolution depending on altitude. In the altitude ranges <
101 8.2, 8.2 - 20.2, 20.2 – 30.1 and >30.1 km the vertical resolution is 30, 60, 180 and 300 m,
102 respectively (Winker et al., 2007, 2010). Here we use data only from the stratosphere,
103 where the tropopause altitude according to MERRA-2 reanalysis (Modern-Era
104 Retrospective analysis for Research and Applications) (Gelaro et al., 2017) was used to
105 discriminate data from the troposphere. Only data recorded during nighttime were used
106 in the general evaluation concerning all the CALIOP data available (Friberg et al., 2018;
107 Martinsson et al., 2022), implying that data will be missing at high latitudes for part of
108 the year with the strongest influence at the summer solstice. Data are also missing at
109 high latitudes mainly in the southern hemisphere due to influence from polar
110 stratospheric clouds. The data were extrapolated linearly to cover all the way to 80°
111 latitude in both hemispheres. In the global perspective used here the fraction of the
112 earth’s surface area affected by the extrapolation is 8.7% at the summer solstice and
113 3.5% two months before/after that time. In most cases the quantitative impact on the
114 global AOD is small, but in special cases, like the eruption of the Icelandic volcano

115 Grimsvötn (64° N) on 21 May 2011, the inability to measure at high latitudes causes
116 larger quantitative errors (Andersson et al., 2015).

117 The evaluation is based on version 4-51 of CALIOP level 1B data (NASA/LARC/SD/ASDC,
118 2024). Clouds within 3km above the tropopause were discriminated based on
119 depolarization of the signal obtained from the CALIOP instrument, polar stratospheric
120 clouds were discriminated based on temperature and data taken in the South Atlantic
121 Anomaly are filtered out as explained in Friberg et al. (2018) and Martinsson et al.
122 (2022). The backscatter data were corrected for attenuation by methodology described
123 in Martinsson et al. (2022) and were first converted to extinction by the standard
124 effective lidar ratio $S = 50$ sr used for CALIOP (Kar et al., 2019). Volcanic eruptions and
125 wildfires with lidar ratio deviating from 50 sr by more than 5% were corrected, see
126 sections 2.3 and 3.4.

127 The stratospheric CALIOP level 3 product (Kar et al., 2019) and the data presented here
128 are both based on the CALIOP level 1B data set but differ with respect to latitude-,
129 longitude- and time-resolution, where CALIOP level 3 is based on monthly averages and
130 we normally use a time-resolution of 1 – 8 days depending on issue investigated. These
131 data sets also differ with respect to lidar ratios: CALIOP level 3 extinction is obtained
132 based on a fixed lidar ratio of 50 sr, whereas we, when possible, estimate effective lidar
133 ratios for aerosol from individual volcanic eruptions and wildfires as described in
134 sections 2.3, 3.1 and 3.4. The notion “effective” relates to that CALIOP is affected by
135 multiple scattering, implying that use of lidar ratios for measurements unaffected by
136 multiple scattering, i.e., the true physical relation between extinction and
137 backscattering of the aerosol studied, will result in overestimation the extinction (Prata
138 et al., 2017; Martinsson et al., 2022). Another difference between CALIOP level 3 and
139 our method is that we correct data for attenuation of the detected scattered light
140 (Martinsson et al., 2022), which is important for identification and quantification of
141 aerosol processes in wildfire aerosol (Martinsson et al., 2022; Friberg et al., 2023) and
142 volcanic aerosol (Martinsson et al., 2025) and to obtain the AOD without influence from
143 attenuation.

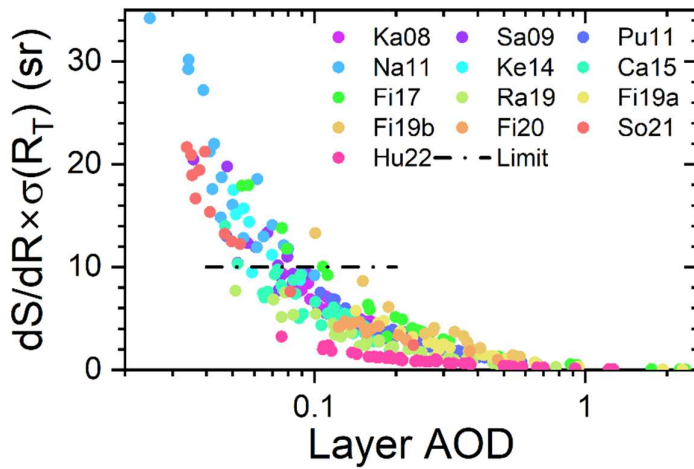
144 **2.2 Estimation of the stratospheric background**

145 The stratospheric aerosol background can rarely be observed in the entire stratosphere.
146 The last time the stratosphere was practically unaffected by injections from volcanic
147 eruptions and wildfires for several years was a few years around the turn of the
148 millennium (Solomon et al., 2011). Still, we need to find means to estimate the
149 stratospheric background because we can estimate the lidar ratio of stratospheric
150 injections from volcanic eruptions and wildfires (presented in next section) but not for
151 the background aerosol. Injections from aerosol events seldom affect the entire
152 stratosphere. Therefore, parts of the stratosphere can be in background conditions
153 when other parts are affected by aerosol injections.

154 To study the background conditions, the stratosphere was subdivided into nine parts
155 spanned by three altitude layers: the lowermost stratosphere (LMS, from the
156 tropopause to the 380 K isentrope, where the latter was obtained from MERRA-2
157 pressures and temperatures), the shallow Brewer-Dobson branch (sBD, between
158 isentropes 380 and 470 K) and the deep Brewer-Dobson branch (dBD, from the 470 K
159 isentrope to 35 km altitude), and three latitude regions: the Southern extratropics
160 (latitudes -80 to -20°), the tropics (latitudes -20 to 20°) and the Northern extratropics
161 (latitudes 20 to 80°)., Data were averaged over 8 days resulting in 46 observations per
162 year in each of the nine stratospheric parts. To estimate the background conditions in
163 this 17-year study, the averages of the three years with the lowest average
164 backscattering of each 8-day period were formed. For two of the nine stratospheric
165 parts, the tropical sBD and dBD, background conditions were rare, wherefore only the
166 two lowest years were used in these two stratospheric parts. The method applied
167 results in the minimum aerosol load observed during the 17-year period. This means
168 that in addition to the tropospheric aerosol and precursor gases entering the
169 stratosphere across the tropical tropopause in the large-scale stratospheric circulation,
170 phenomena such as the ATAL (Vernier et al., 2015) and other exchanges across the
171 extratropical tropopause are included in the background.

172 The extracted lowest 8-day values formed a seasonal pattern that was fitted by the sum
173 of a constant and a sinusoidal function. These fits were used to express the average
174 backscattering of the background aerosol in each of the nine stratospheric parts over
175 the 17 years spanned by CALIOP measurements. The average backscattering converts

176 to AOD when multiplied with the lidar ratio. The fitted background was subtracted from
 177 the measured total backscattering to form the backscattering from volcanic eruptions
 178 and wildfires. These background-subtracted average backscattering data were
 179 converted to AOD via the lidar ratios obtained from individual aerosol events, as
 180 described in the next section.



181

182 **Figure 1.** Relation between the layer AOD and the measure on the uncertainty of the
 183 lidar ratio estimation. dS/dR is the sensitivity of the lidar ratio (S) to small shifts of the
 184 target scattering ratio (R) and $\sigma(R_T)$ is the standard deviation of the target R of each
 185 eruption or wildfire obtained horizontally beside each aerosol layer investigated. Layers
 186 with uncertainty exceeding 10 sr (“limit”) are discarded in the following analysis.

187 **2.3 Lidar ratio**

188 The lidar ratio of the aerosol from the strongest volcanic eruptions and wildfires in the
 189 period studied was estimated based on methodology described in Martinsson et al.
 190 (2022), where individual dense aerosol layers are investigated. In that method a target
 191 value in scattering ratio (R) obtained horizontally beside the studied aerosol layer (R_T) is
 192 reached below the layer in an iterative procedure that results in an estimate of the
 193 effective lidar ratio, while correcting for attenuation of the backscattered signal. The
 194 effective lidar ratio obtained describes the average conditions of the entire layer where
 195 the optical properties in principle can vary. However, the lidar ratio estimates are
 196 obtained in dense aerosol layers, where the influence from background aerosol is small.

197 The uncertainty in the estimated lidar ratio depends on the AOD of the layer. A small
198 change in the lidar ratio (S) results in a substantial change in the scattering ratio (R)
199 below a dense layer, i.e., dS/dR is small for dense aerosol layers. dS/dR is obtained by
200 shifting R slightly around R_T . There is also an uncertainty in how well R_T represents the
201 aerosol beneath the layer. We estimate that uncertainty by the standard deviation of the
202 scattering ratio ($\sigma(R_T)$) obtained horizontally beside all the aerosol layers studied for
203 each volcanic eruption or wildfire. This is thus based on the assumption that the aerosol
204 horizontally beside and below the aerosol layer have the same standard deviation in R ,
205 but the actual scattering ratios horizontally beside and below an individual layer are
206 uncorrelated. The estimated uncertainty becomes $dS/dR \times \sigma(R_T)$. Figure 1 shows all
207 $dS/dR \times \sigma(R_T)$ related to the AOD of all the estimations of the lidar ratio. The uncertainty in
208 the lidar ratio estimate increases as the layer AOD decreases, hence a limit was set to
209 $dS/dR \times \sigma(R_T) < 10$ sr to pass as a lidar ratio estimate. As a result, most estimates for
210 three volcanic eruptions, 2011 Nabro (Na11), 2014 Kelut (Ke14), and 2021 Soufriere
211 (So21), among the 12 eruptions and wildfires analyzed were lost, as illustrated in Figure
212 1.

213 For simplicity all the CALIOP data were evaluated using the standard lidar ratio of $S_0 =$
214 50 sr in the general evaluation. In the study of individual aerosol layers (Figure 1) both
215 the AOD based on the estimated lidar ratio and that based on S_0 were computed, where
216 the latter (AOD_{50}) was used to obtain the deviation caused by using S_0 . This deviation
217 depends on the S/S_0 ratio and AOD_{50} , where the effect of S/S_0 is the dominant one
218 except for very dense aerosol layers. The result from the general evaluation is corrected
219 afterwards based on the ratio of S_0 and the estimated S , see section 3.4.

220 **3. Results**

221 Here we will present the stratospheric aerosol from the troposphere to 35 km altitude
222 and the latitude range -80 to 80° in the era of lidar measurements by the CALIOP
223 instrument aboard the CALIPSO satellite. CALIOP measured the backscattered intensity
224 from a 532 nm laser beam, which can be converted to extinction by multiplying with the
225 ratio of extinction to backscatter, i.e. the lidar ratio. Knowing the lidar ratio thus is
226 central for quantification by obtaining AOD from CALIOP measurements. We developed

227 methodology to estimate the effective lidar ratio from CALIOP measurements, a
 228 methodology that also corrects for attenuation of the laser signal (Martinsson et al.,
 229 2022). Here we start by presenting the lidar ratio of the main aerosol events of the
 230 CALIOP era before giving an overview of the AOD in the period studied. Then we
 231 investigate separation of aerosol signals of aerosol events due to volcanic eruptions and
 232 wildfires from signals due to stratospheric background aerosol. This is followed by
 233 sections on corrections of AOD due to lidar ratio deviations from the commonly
 234 assumed 50 sr, an overview of the AOD and a simplified estimate of the stratospheric
 235 aerosol's radiative impact.

236 **3.1 Lidar ratio**

237 The main aerosol events affecting the stratosphere in the CALIOP era are presented in
 238 Table 1. The methodology we use to estimate lidar ratios requires sufficiently dense
 239 aerosol layers as described in section 2, implying that some of the events mentioned in
 240 Table 1 are not suitable for the methodology. The lidar ratio was investigated for

241 **Table 1.** Major volcanic eruptions and wildfires affecting the stratospheric aerosol in the
 242 CALIOP era.

| | Date | Volcano/wildfire | Lat ^a | Lon ^b | SO ₂ (Tg) | References |
|----|---------------------------|-------------------------------|------------------|------------------|----------------------|------------------------|
| | <i>Volcanic eruptions</i> | | | | | |
| 1 | 2006-05-20 | Soufriere Hills (Su) | 17° | -62.2° | 0.2 | Carn and Prata (2010) |
| 2 | 2006-10-07 | Rabaul (Rb) | -4° | 152° | 0.23 | Carn et al. (2009) |
| 3 | 2008-08-07 | Kasatochi (Ka) | 52° | -176° | 1.7 | Thomas et al. (2011) |
| 4 | 2009-06-12 | Sarychev (Sa) | 48° | 153° | 1.2 | Haywood et al. (2010) |
| 5 | 2010-10-05 | Merapi (Me) | -7° | 110° | 0.44 | Surono et al. (2012) |
| 6 | 2011-06-05 | Puyehue-Cordón Caulle (Pu) | -40° | -72° | 0.25 | Clarisse et al. (2012) |
| 7 | 2011-06-12 | Nabro (Na) | 13° | 42° | 1.5 | Clarisse et al. (2012) |
| 8 | 2014-02-13 | Kelut (Ke) | -8° | 112° | 0.18 | Li et al. (2017) |
| 9 | 2015-04-23 | Calbuco (Ca) | -41° | -73° | 0.3 | Pardini et al. (2018) |
| 10 | 2018-07-27 | Ambae (Am) | -15° | 168° | 0.36 | Malinina et al. (2021) |
| 11 | 2019-06-22 | Raikoke (Ra) | 48° | 153° | 1.5 | Kloss et al. (2021) |
| 12 | 2019-06-26 | Ulawun (Ul) | -5° | 151° | 0.14 | Kloss et al. (2021) |
| 13 | 2019-08-03 | Ulawun (Ul) | -5° | 151° | 0.3 | Kloss et al. (2021) |
| 14 | 2021-04-10 | Soufriere (So) | 13° | -61° | 0.31 | Taylor et al. (2023) |
| 15 | 2022-01-15 | Hunga Ha'apai (Hu) | -21° | 175° | 0.45 | Carn et al. (2022) |
| | <i>Wildfires</i> | | | | | |
| 16 | 2006-12-19 | Australia (A1) | -37° | 147° | - | McCarthy et al. (2012) |

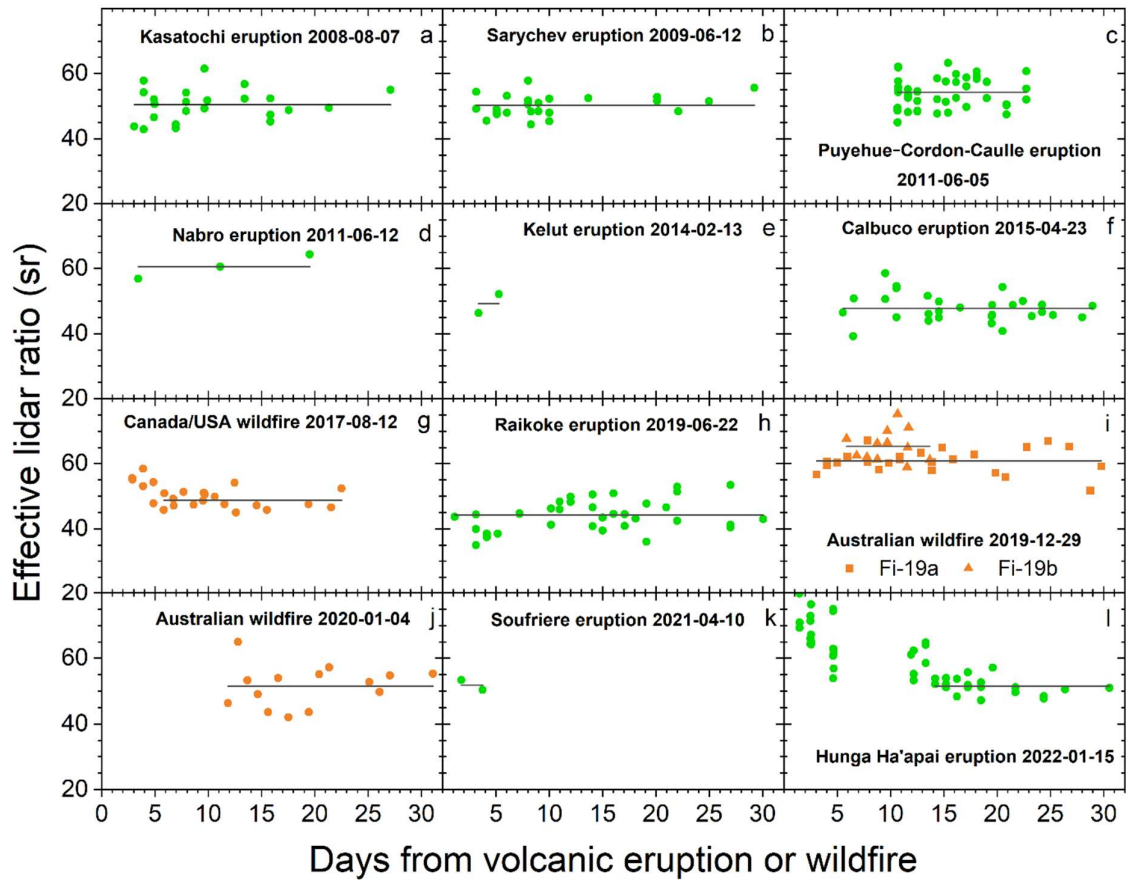
| | | | | | | |
|----|------------|-----------------|------|-------|---|------------------------|
| 17 | 2009-02-07 | Australia (A2) | -38° | 146° | - | Cruz et al. (2012) |
| 18 | 2017-08-12 | Canada/USA (CU) | 53° | -123° | - | Fromm et al. (2021) |
| 19 | 2019-12-29 | Australia (A3) | -37° | 149° | - | Peterson et al. (2021) |
| 20 | 2020-01-04 | Australia (A4) | -37° | 149° | - | Peterson et al. (2021) |

243

244 stratospheric aerosol from nine volcanic eruptions and three wildfire events (Figure 2).
 245 For some of these aerosol events the screening related to the uncertainty in the
 246 estimated lidar ratio (Figure 1) resulted in few observations, namely for the 2011 Nabro,
 247 2014 Kelut and the 2021 Soufriere eruptions. Most of the eruptions and wildfires display
 248 a stable lidar ratio during the first month, whereas two of the events show an initial
 249 decrease of the lidar ratio, the 2017 North American wildfire (Figure 2g) and the 2022
 250 Hunga Ha'apai eruption (Figure 2l), towards a stable value.

251 Effective lidar ratios are presented here which are best suited for application to
 252 measurements that, like CALIOP, are affected by multiple scattering (Martinsson et al.,
 253 2022). Compared with previous estimates, the results presented here are approximately
 254 20% lower than those of Prata et al. (2017) for the Kasatochi, Sarychev and Puyehue-
 255 Cordon Caulle eruptions, who estimated lidar ratio for measurements that are not
 256 affected by multiple scattering. Ohneiser et al. (2020) present Raman lidar measurements of
 257 the 2019 Australian wildfire (Table 1) that are not affected by multiple scattering. On 2020-01-09
 258 around 04:00 UTC (longitude -70.9, latitude -53.2) $S = 76$ sr was obtained. The closest CALIOP
 259 measurement in space and time that we evaluated was taken on the same day at 04:05,
 260 position (-43.4, -53.1) with $S = 75$ sr. The day before, at position (-57.2, -50.0) $S = 70$ sr and the
 261 day after at position (-55.0, -57.1) $S = 71$ sr. All these three measurements belong to the fires
 262 taking place last days of 2019, category B (outside the vortex) and are the three highest effective
 263 lidar ratios obtained in this category.

264 Stratospheric aerosol resulting from most volcanic eruptions and wildfires have a lidar
 265 ratio close to 50 sr, which is the commonly used lidar ratio for CALIOP data (Kar et al.,
 266 2019). Notable exceptions with lidar ratio deviating by more than 5% from 50 sr are the
 267 ash-dominated 2011 eruption of Puyehue-Cordón Caulle (Figure 2c), the 2019



268

269 **Figure 2.** Effective particle lidar ratios the first 30 days after a volcanic eruption or
 270 wildfire with a line displaying the average of each event. All measurements concurring
 271 with the condition $dS/dR \times \sigma(R) < 10$ are displayed for a) Kasatochi eruption 2008-08-07,
 272 b) Sarychev eruption 2009-06-12, c) Puyehue-Cordón-Caulle eruption 2011-06-05, d)
 273 Nabro eruption 2011-06-12, e) Kelut eruption 2014-02-13, f) Calbuco eruption 2015-04-
 274 23, g) Canada/USA wildfire 2017-08-12, h) Raikoke eruption 2019-06-22, i) Australian
 275 wildfire, 2019-12-29 subdivided in part Fi-19a (observations in the vortex (Kablik et al.,
 276 2020)) and Fi-19b (observations outside the vortex), j) Australian wildfire 2020-01-04, k)
 277 Soufriere eruption 2021-04-10 and l) Hunga Ha'apai eruption 2022-01-15. The averages
 278 include all data points except for the Canada/USA wildfire and the Hunga Ha'apai
 279 eruption where the initial decline in the lidar ratio is not part of the average represented
 280 by horizontal lines.

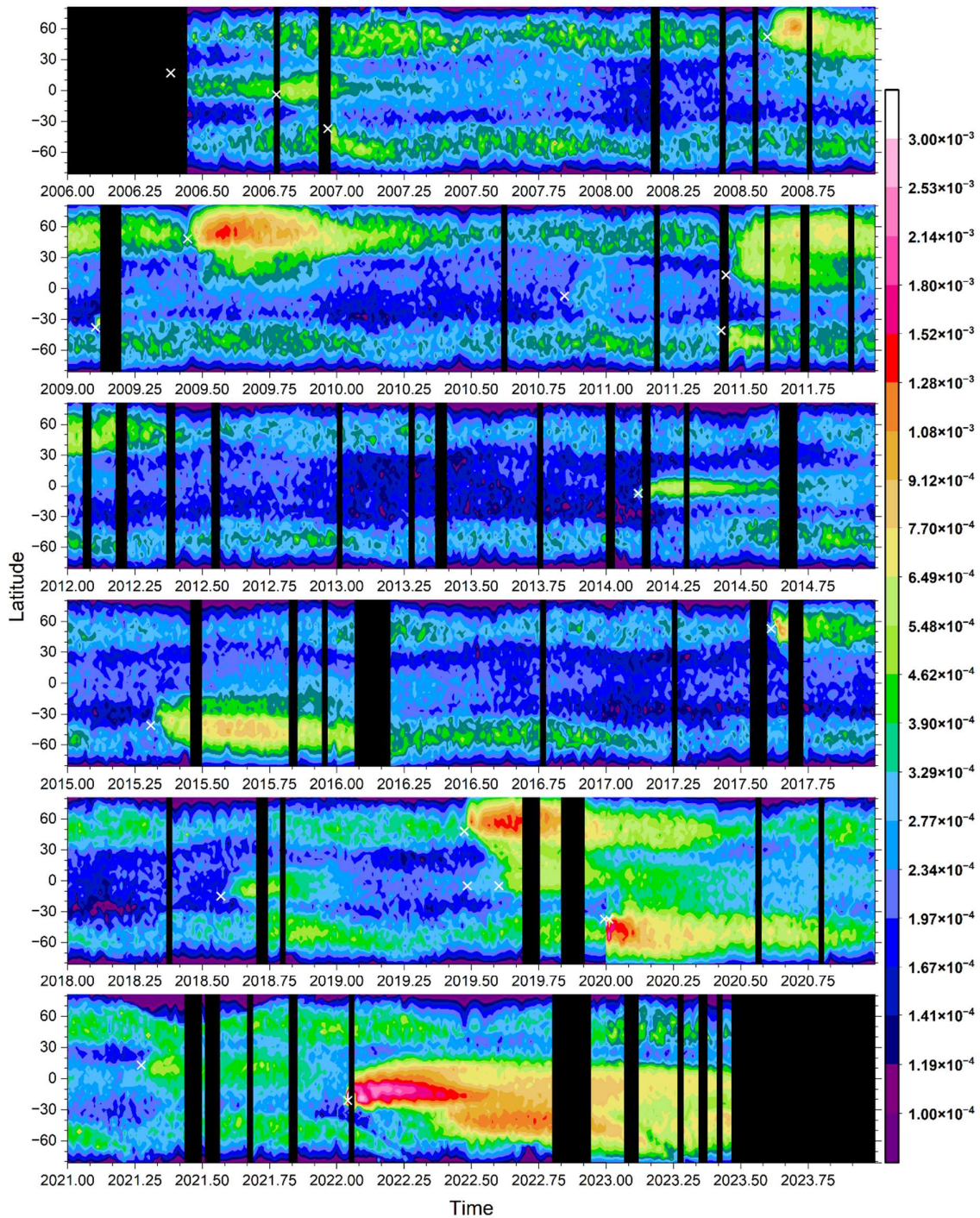
281

282 Raikoke eruption (Figure 2h) and the Australian wildfire in the last days of 2019 (Figure
283 2i). Also, the 2011 Nabro eruption (Figure 2d) tends to deviate from the commonly
284 adopted lidar ratio of 50 sr of stratospheric aerosol, however the observations are too
285 few for a firm conclusion. In the forthcoming presentation the lidar ratio of 50 sr will be
286 used before the influence from deviations is addressed in sections 3.4 and 3.5.

287 **3.2 Stratospheric aerosol events overview**

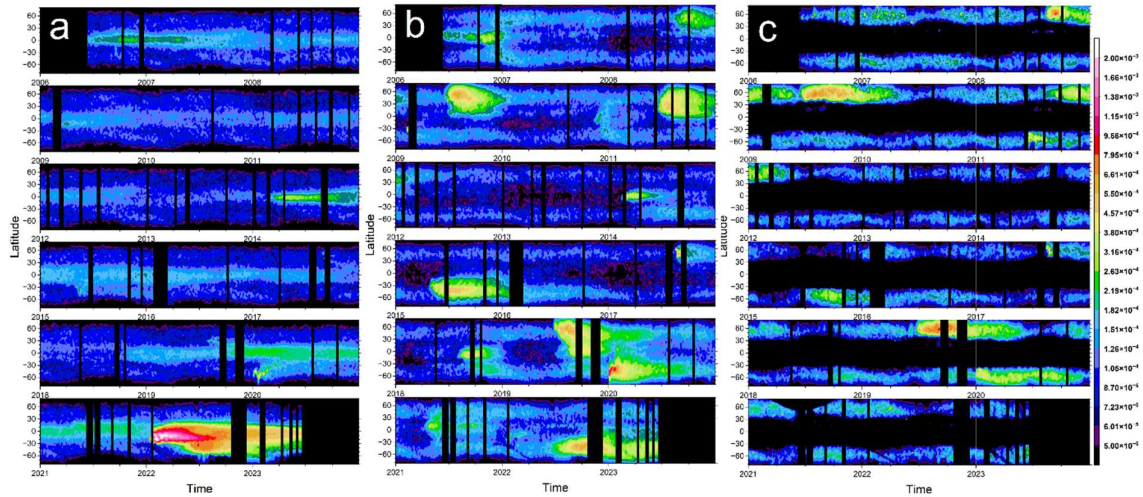
288 At least 15 volcanic eruptions and 5 wildfires clearly affected the stratospheric aerosol
289 in the CALIOP era (Table 1). The latitude distribution of the stratospheric aerosol from
290 the tropopause to 35 km altitude is shown in Figure 3, and subdivided into three layers,
291 dBD, sBD, and LMS, in Figure 4 with full size versions in supplementary Figures S1 – S3.
292 Additionally, the altitude distribution is shown in three latitude ranges (-80 to -20°, -20 to
293 20° and 20 to 80°) in Figure 5 (supplementary Figures S4 – S6).

294 The influence from injections of aerosol from volcanic eruptions and wildfires has
295 durations of a few months to several years (Friberg et al., 2018). The latter category is
296 the aerosol events that enter the dBD branch in the tropics. The outstanding event
297 fulfilling this requirement in the period studied is the submarine eruption of Hunga
298 Ha’apai in 2022 (Figures 4a and 5a, b) where intense volcanism – sea interaction
299 (Seabrook et al., 2023; Mastin et al., 2024) formed large quantities of stratospheric
300 aerosol, whereas aerosol formation from SO₂ could explain only ~30% of the AOD
301 (Martinsson et al., 2025). The remaining aerosol events in the dBD have much lower
302 AODs. The Kelut eruption in 2014 affected the dBD for approximately 4 years. The
303 combined effect of the 2006 eruptions of Soufriere Hills and Rabaul (Figure 5b) show
304 similar long-term effects on the dBD in the tropics (Figure 4a). The combined effects of
305 4 volcanic eruptions, the 2018 Ambae, the two 2019 Ulawun and the 2021 Soufriere
306 eruptions, gradually increased the dBD aerosol load in the tropics. In addition to these
307 tropical eruptions, some extratropical aerosol events affected the dBD: the 2015
308 Calbuco eruption and some plumes injected above the main aerosol layer of the 2019
309 Raikoke eruption. Three wildfires also contributed aerosol to the extratropical dBD, the
310 2009 Australian, the 2017 Canada/USA and the 2019 Australian wildfires. The aerosol
311 from the latter fire formed a vortex where



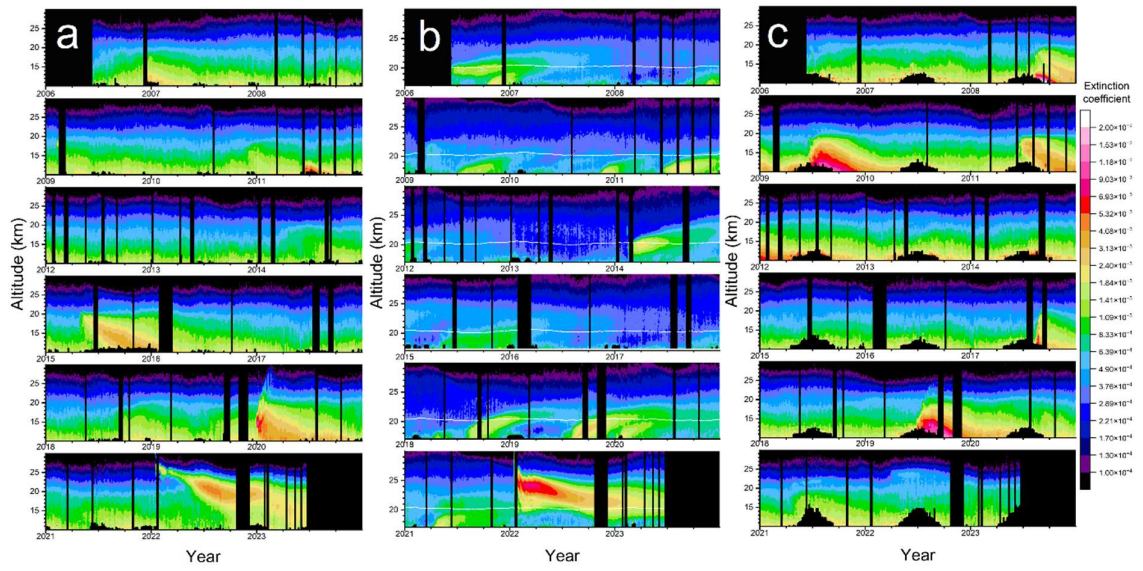
312

313 **Figure 3.** AOD integrated from the tropopause to 35 km altitude averaged over 4 days
 314 and 3 degrees in latitude. The lidar ratio is set to 50 sr. Color scale: The data is latitude
 315 weighted in the way that the global AOD contribution per degree of latitude is shown, i.e.
 316 the sum over latitude is the total AOD at any given time. The data has been extrapolated
 317 at high latitudes as described in section 2.1, Figure S7 shows the data without
 318 extrapolation. White crosses indicate time and latitude of aerosol events mentioned in
 319 Table 1.



320

321 Figure 4. AOD integrated in three layers: a) dBD, b) sBD and c) LMS. The color scale is
 322 latitude weighted as explained in the caption of Figure 3. Full size images are displayed
 323 in the Supplementary material, Figures S1 – S3.



324

325 Figure 5. Extinction coefficients (km^{-1}) averaged in three latitude bands: a) southern
 326 extratropics (-80 to -20°), b) tropics (-20 to 20°) and c) northern extratropics (20 to 80°).
 327 Full size images are displayed in the Supplementary material, Figures S4 – S6.

328

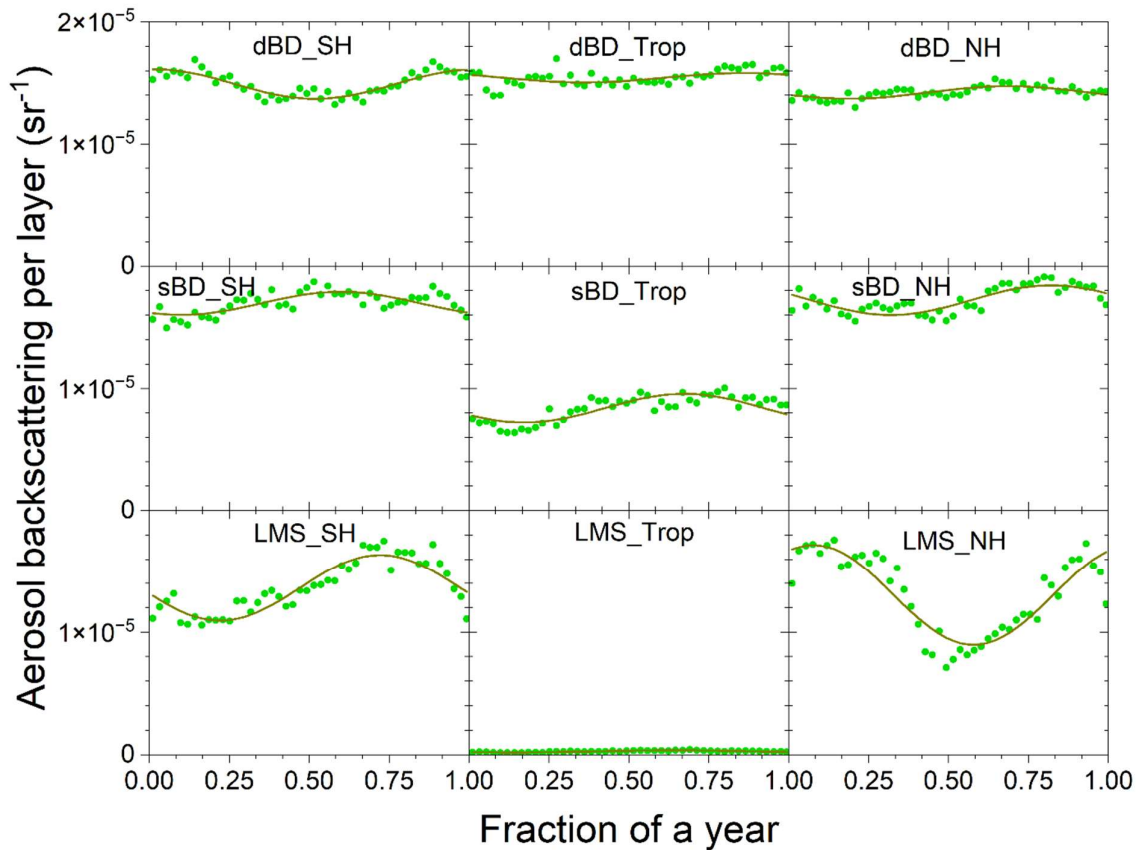
329 the aerosol rose above 31 km altitude (Kablick et al., 2020). The extratropical aerosol
 330 events leave the dBD faster than the tropical ones because of the extratropical
 331 downward motion of the BD circulation.

332 The shallow Brewer-Dobson (sBD) branch (Figure 4b) displays no such strong aerosol
333 event as the effect of the 2022 Hunga Ha’apai eruption on the dBD (Figure 4a). On the
334 other hand, many events had intermediate or small impacts. The Australian wildfires at
335 the end of 2019 and the beginning of 2020 made an initial strong impact that was rapidly
336 reduced by loss of 90% of the aerosol with a half-life of 10 days, likely due to photolysis
337 of organic aerosol (Friberg et al., 2023), as did the 2017 North American wildfire but with
338 a lower aerosol load (Martinsson et al. 2022) and, to a still lower extent, the 2009
339 Australian wildfire. The main volcanic eruptions affecting the sBD branch were the 2008
340 Kasatochi, 2009 Sarychev, 2011 Nabro, 2015 Calbuco, 2019 Raikoke and, after a delay
341 due to transport from the dBD branch, the 2022 Hunga Ha’apai eruptions (Figure 4a, b).
342 Other volcanos with smaller impact on the sBD branch were the 2006 Soufriere Hills
343 and Rabaul, the 2010 Merapi, 2014 Kelut, 2018 Ambae, 2019 Ulawun (2 eruptions) and
344 2021 Soufriere eruptions.

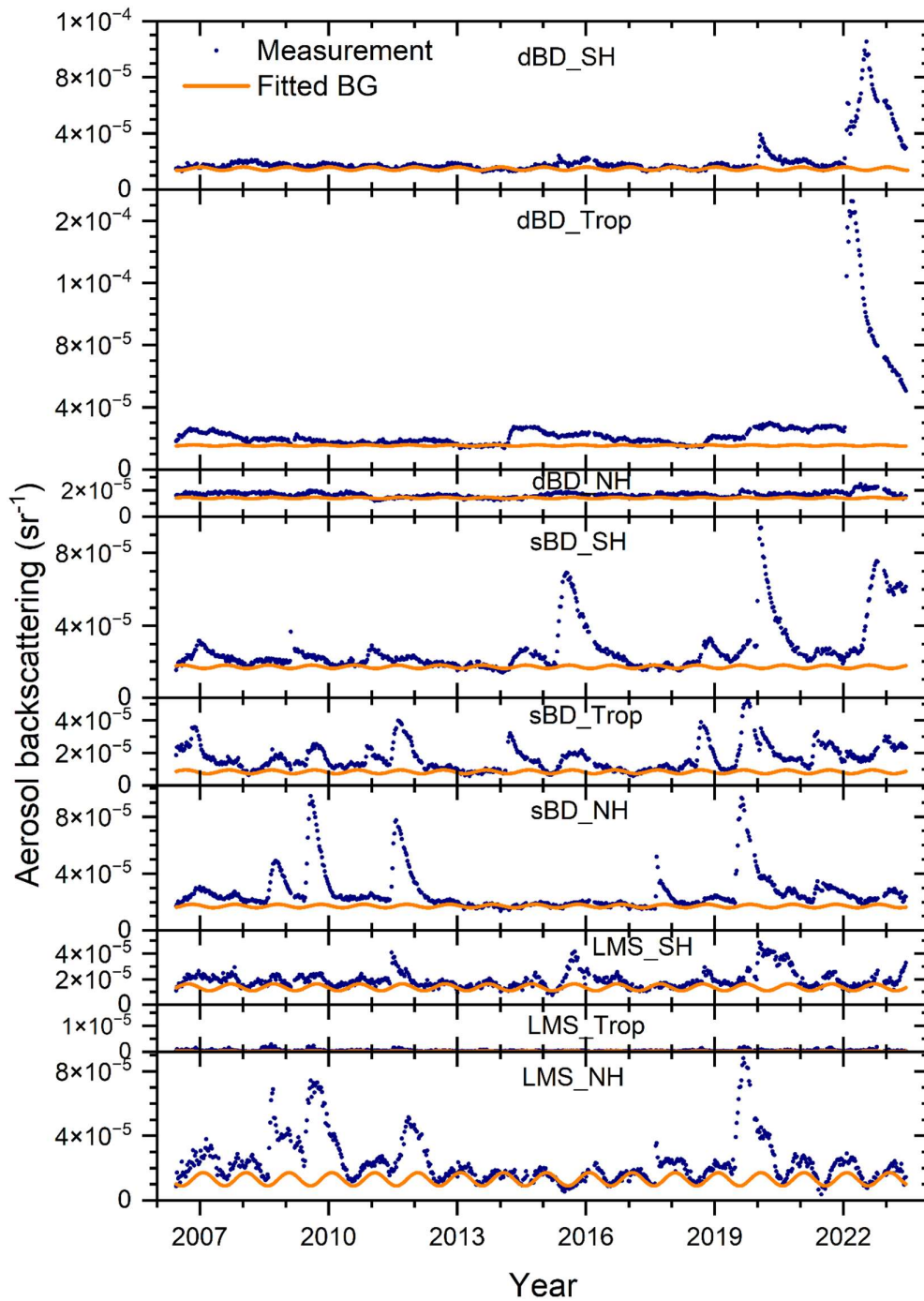
345 The LMS (Figure 4c), the last stratospheric part passed by the air and its trace
346 substances in the large-scale stratospheric circulation before exiting to the
347 troposphere, is affected by all stratospheric aerosol events. In addition, some
348 extratropical aerosol events do not reach beyond the LMS. The Kasatochi eruption
349 resulted in two distinct aerosol layers, a thin layer in the sBD whereas the main part of
350 its effluents was injected both sides of and close to the tropopause (Andersson et al.,
351 2015). Other exclusive LMS events in the period studied here are the 2011 Puyehue-
352 Cordón Caulle eruption and the 2006 Australia wildfire.

353 Most volcanic eruptions show a gradual increase in AOD over few months before
354 reaching its maximum because of the time required for aerosol dynamical processing
355 and to transform sulfur dioxide into sulfate, which usually is the main component of the
356 aerosol from volcanic eruptions. Notable exceptions are the 2022 Hunga Ha’apai and
357 the 2011 Puyehue-Cordón Caulle eruptions (Figure 3). The aerosol of the latter eruption
358 mainly consisted of volcanic ash (Vernier et al., 2013) and the former by aerosol
359 containing sulfate and sea-salt from volcanism – sea interaction (Martinsson et al.,
360 2025). These eruptions are thus less influenced by delay in aerosol formation from
361 chemical transformation. The wildfires in the years 2009, 2017, 2019 and 2020 also

362 rapidly reach the maximum AOD before a decline due to photolysis of organic
 363 compounds reduces the AOD by 90% (Martinsson et al., 2022; Friberg et al., 2023).



364
 365 **Figure 6.** Average backscattering, which when multiplied with the lidar ratio becomes
 366 the AOD of the layer, of the background aerosol extracted based on the three lowest
 367 average values of each 8-day period over the year in the CALIOP era (2006 – 2023). The
 368 extracted data were fitted to a constant and a sinusoidal function. (Exceptions: the two
 369 lowest 8-day averages were used for “dBD_Trop” and “sBD_Trop” due to infrequent
 370 background values.) The extraction was undertaken in nine regions spanned by
 371 latitudes: -80 to -20° (SH), -20 to 20° (Tropics), 20 to 80° (NH) and altitude ranges: the
 372 tropopause to 380 K isentrope (LMS), 380 to 470 K isentrope (sBD), 470 K to 35 km
 373 altitude (dBD). The data were latitude weighted in the way that the sum of the nine
 374 layers is the global aerosol backscattering.



375

376 **Figure 7.** Stratospheric aerosol average backscattering, which when multiplied with the
 377 lidar ratio becomes the AOD, and fitted background in nine latitude and altitude regions:
 378 the deep BD branch (470 K isentrope to 35 km altitude), the shallow BD branch
 379 (between isentropes 380 and 470 K) and the LMS (from the tropopause to the 380 K
 380 isentrope) and three latitude regions the southern hemisphere extratropics (-80 to -20°),
 381 the tropics (-20 to 20°) and the northern hemisphere extratropics (20 to 80°) to find time-
 382 sections not or weakly affected by stratospheric aerosol events (see Fig. 4 and text for
 383 details).

384

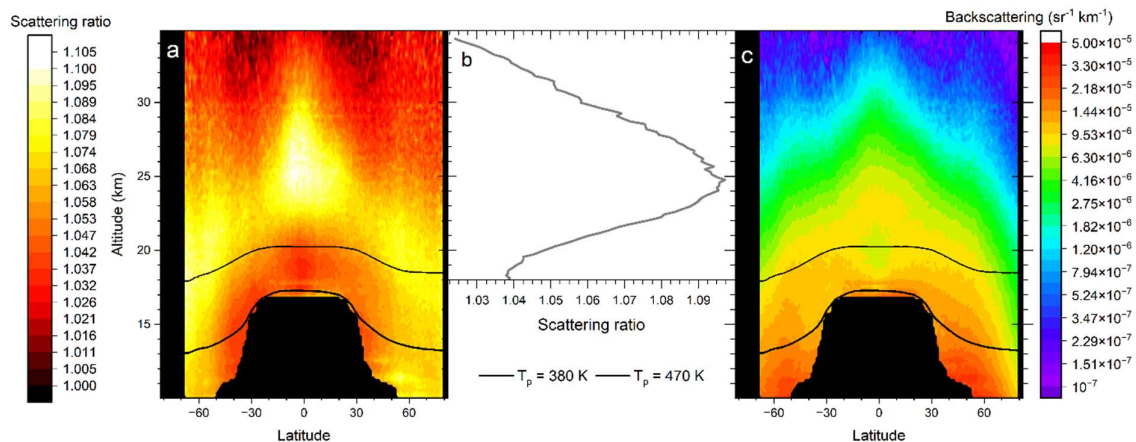
385 **3.3 Stratospheric background**

386 The stratospheric background aerosol is not a well-defined concept. One way is to
387 include all but major aerosol events in the background to obtain a persistently variable
388 background (Solomon et al., 2011). An alternative background is based on SAGE II
389 measurements in the volcanically quiescent period in the late 1990s to early 2000s
390 (Kremser et al., 2016). CALIOP measurements were not available in those years. A
391 volcanic eruption or wildfire rarely affects the entire stratosphere. Therefore, we divided
392 the stratosphere into nine sections by altitude and latitude thereby increasing the
393 probability of finding conditions close to background separately in each of the layers
394 using the average of the three lowest average backscattering values (in two cases the
395 two lowest) of each layer over the year (Figure 6), as described in the methods section.

396 The distribution of aerosol over the nine layers used to extract the background aerosol is
397 shown in Table 2. Seven of the nine layers each contain 11 – 15% of the background
398 aerosol in the stratosphere from the tropopause to 35 km altitude during conditions that
399 are close to background. The smallest contribution comes from the tropical LMS, which
400 is to be expected given the small air volume of that layer. The tropical sBD also has a
401 small contribution, but that cannot be explained by the air volume. This layer where
402 tropospheric air enters the stratosphere extends to approximately 20 km altitude, where
403 UV radiation intensity is too weak to efficiently oxidize carbonyl sulfide (Weisenstein et
404 al., 1997), which is an important precursor gas of the stratospheric background aerosol
405 (Crutzen, 1976; Kremser et al., 2016), a topic we return to below. Seasonal changes in
406 aerosol background average backscattering are most pronounced in the extratropical
407 LMS, especially in the NH. The volume of LMS varies over the year. That variation
408 (Appenzeller et al., 1996) approximately coincides with the variation in Figure 6 both in
409 terms of seasonality and the stronger amplitude in the LMS of the NH. In addition to the
410 size of the LMS, seasonality of the backscattering intensity is connected to a variability
411 in aerosol load. Poleward transport in the BD circulation maximizes in the winter
412 resulting in increased extratropical downward motion of the stratospheric aerosol layer
413 in the spring resulting in low aerosol load in the summer LMS when the mass transport
414 across its upper boundary is at its minimum. The latter also coincides with the

415 weakening of the subtropical Jetstream which increases the tropospheric influence on
 416 the LMS. In the summer/early fall there is also influence from ATAL (Vernier et al., 2015)
 417 and small wildfires briefly affecting the stratosphere (Peterson et al., 2025). The
 418 chemical composition of the LMS aerosol of the Northern hemisphere in that period
 419 differs from winter/spring/early summer by having a larger carbon than sulfur content
 420 (Martinsson et al., 2019). The change in composition can be caused by the ATAL and/or
 421 small wildfires which thus contribute to the effect of the large-scale stratospheric
 422 circulation in the build-up of the NH LMS aerosol load during late summer and fall.

423 The average backscattering of the stratospheric aerosol and the estimated background
 424 (Figure 6) in nine altitude and latitude layers is shown in Figure 7. By comparing these
 425 two quantities, we verify the underlying assumption in the method used to obtain the
 426 background that the stratospheric aerosol background has no long-term trend, which
 427 agrees with previous observations (Kremser et al., 2016). Subtracting the background,



428

429 **Figure 8.** The stratospheric aerosol averaged over year 2013, which was close to
 430 background conditions. a) The scattering ratio, i.e., the ratio between the total to the
 431 modeled backscattering of air molecules. This intensive parameter is not latitude
 432 weighted. b) Average scattering ratio in the central tropics (latitudes -10 to 10°)
 433 dependence on altitude. c) Average aerosol backscattering, this extensive quantity is
 434 latitude weighted. Black lines in a) and c) are the yearly average positions of the
 435 potential temperatures (T_p) 380 and 470 K.

436

437 we obtain the average backscattering from volcanic eruptions and wildfires. The net
 438 average backscattering of the layers was converted to AOD of the layers by

439 multiplication with the lidar ratio of 50 sr in Figure S8 with contributions from volcanic
 440 eruptions and wildfires as described in section 3.2.

441 Except for a tiny peak in the LMS in the Northern extratropics, 2013 is close to
 442 background conditions (Figure 7). The stratospheric background aerosol is often
 443 thought of as a layer located above 20 km altitude in the tropics and lower in the
 444 extratropics. This is approximately true in terms of scattering ratio (R), the optical
 445 equivalent of mixing ratio (Figure 8a). More than half of the air entering the tropical
 446 stratosphere is transported polewards in the sBD (Lin and Fu, 2013), where the
 447 scattering ratio remains low in a band closest to the tropopause (Figure 8a). This band
 448 contains young stratospheric air compared to air at the same altitude but at higher
 449 latitude (Austin and Li, 2006; Butchart, 2014; Ploeger et al., 2021). In the air rising
 450 further in the tropical stratosphere a dramatic increase of the aerosol mixing ratio can
 451 be seen above 20 km altitude. The aerosol signal increases by a factor 2.5 (Figure 8b)
 452 from 19 to 25 km altitude in the latitude range -10 to 10°, i.e., 70% of the aerosol at 25
 453 km is formed above 19 km altitude. The dBD air is transported polewards and descends
 454 at higher latitudes than the sBD air (Figure 8a). With a typical vertical

455 **Table 2.** Average backscattering of background aerosol and AOD of aerosol events in
 456 2006 - 2023 and the distribution over nine stratospheric layers.

| Backscattering background ^a | | | | |
|--|---------------|-----|---------|-----|
| | <i>Global</i> | SH | Tropics | NH |
| <i>Total</i> | | 40% | 21% | 39% |
| dBD | 39% | 13% | 14% | 12% |
| sBD | 37% | 15% | 7.3% | 15% |
| LMS | 24% | 12% | 0.2% | 11% |

| AOD aerosol events ^b | | | | |
|---------------------------------|---------------|------|---------|------|
| | <i>Global</i> | SH | Tropics | NH |
| <i>Total</i> | | 33% | 31% | 35% |
| dBD | 31% | 9.0% | 18% | 4.0% |
| sBD | 43% | 15% | 13% | 15% |
| LMS | 26% | 9.0% | 0.4% | 17% |

457 ^aAverage backscattering of background = 0.00011 sr⁻¹

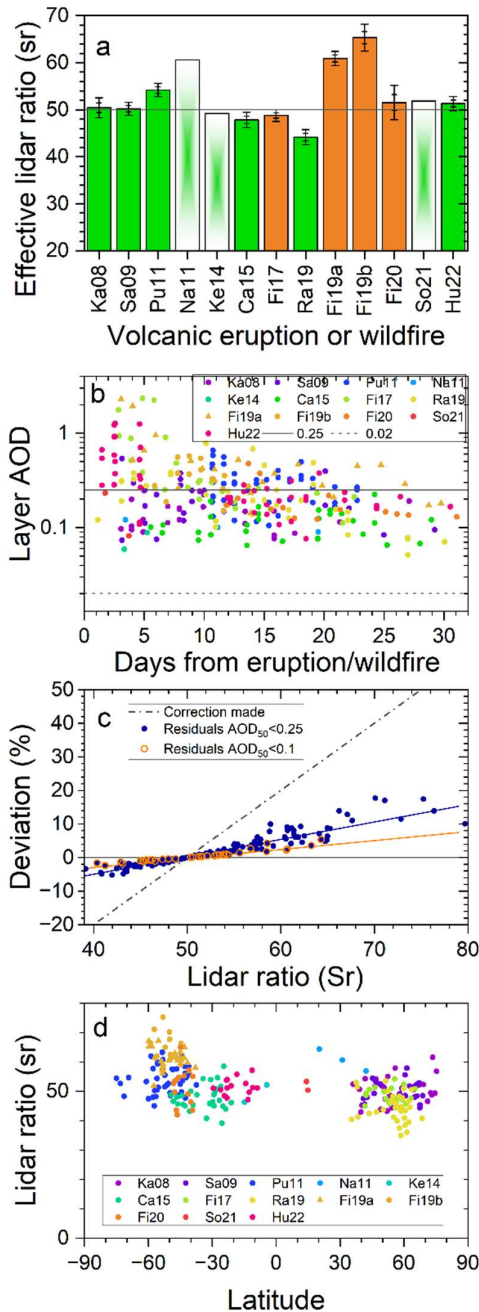
458 ^bAverage AOD from aerosol events (2006 – 2023) = 0.0031

459

460 velocity of 20 m/day (Mote et al., 1998) the transport from the tropical tropopause (at 17
 461 km) to 19 km altitude requires approximately 100 days, providing ample time for

462 conversion of SO₂ before reaching the latter altitude (Nicknisch et al., 2025). Hence, little
463 SO₂ enters the dBD, implying particle formation from another source. Intensifying UV
464 radiation with altitude causes oxidation of the most abundant sulfur compound in the
465 atmosphere, i.e., carbonyl sulfide (OCS) (Crutzen, 1976; Kremser et al., 2016), whereas
466 this compound remains intact in the sBD. The requirement of intense UV radiation for
467 oxidation makes OCS an important aerosol formation pathway mainly in the dBD. The
468 formed aerosol is transported polewards where downward transport brings the aerosol
469 to the sBD and LMS layers before the transport out of the stratosphere (Figure 8a). The
470 formation pathways of the stratospheric background aerosol are still debated. The
471 estimated contribution of OCS to the stratospheric background aerosol ranges from 20
472 – 50% (Sheng et al., 2015; Chin and Davies, 1995) to 70% or more (Crutzen, 1976; Brühl
473 et al., 2012). High-resolution lidar data, like that of CALIOP, can be used to constrain
474 modeling efforts to quantify sulfurous aerosol sources by reconstructing the CALIOP
475 observations in Figure 8 to understand the sources of the background aerosol.

476 When instead considering the absolute background aerosol load (Figure 8c) we find the
477 highest aerosol load at low stratospheric altitudes. The air in the Brewer-Dobson



478

479 **Figure9.** a) Average lidar ratios according to Fig. 2 with standard errors and 95% ranges
 480 of volcanic eruptions and wildfires. Too few observations for error estimations were
 481 obtained for the eruptions of Nabro (Na11), Kelut (Ke14) and Soufriere (So21). b) AODs
 482 of aerosol layers with $dS/dR \times \sigma(R) < 10$ sr Vs. time from the eruption or wildfire. The full
 483 line illustrates approximate maximum layer AOD after 1 month, and the broken line
 484 indicates the approximate maximum layer AOD observable by limb-viewing techniques
 485 (note: logarithmic y-scale). c) Correction of AOD obtained by setting the lidar ratio to 50
 486 sr (AOD_{50}), based on a linear dependence of the AOD on the lidar ratio. The residual
 487 deviation after the correction of two categories is also shown: aerosol layers with AOD_{50}
 488 < 0.1 and < 0.25 . d) Estimated lidar ratios in Figure 2 Vs. latitude.

489 circulation becomes compressed during the downwelling in the extratropics in
490 accordance with the altitude-dependence of the atmospheric pressure. Mixing across
491 the extratropical tropopause culminating in the late summer with the ATAL affects the
492 aerosol load in the LMS but does not affect the mixing ratios appreciably (Figure 8a).
493 However, somewhat higher scattering ratios are found in the ATAL region (15 – 45° N and
494 13 – 18 km altitude (Vernier et al., 2015)) compared with the same region of the
495 southern hemisphere. In monthly resolution, rather than the yearly resolution of Figure
496 8, enhanced aerosol load in the ATAL area is clearly visible in July – September 2013
497 (Martinsson et al., 2017). During background conditions approximately 60% of the
498 aerosol backscattering signal (AOD divided by the lidar ratio) is found in the two lower
499 layers, sBD and LMS (Table 2), containing aerosol transported from both the sBD and
500 dBD of the tropics.

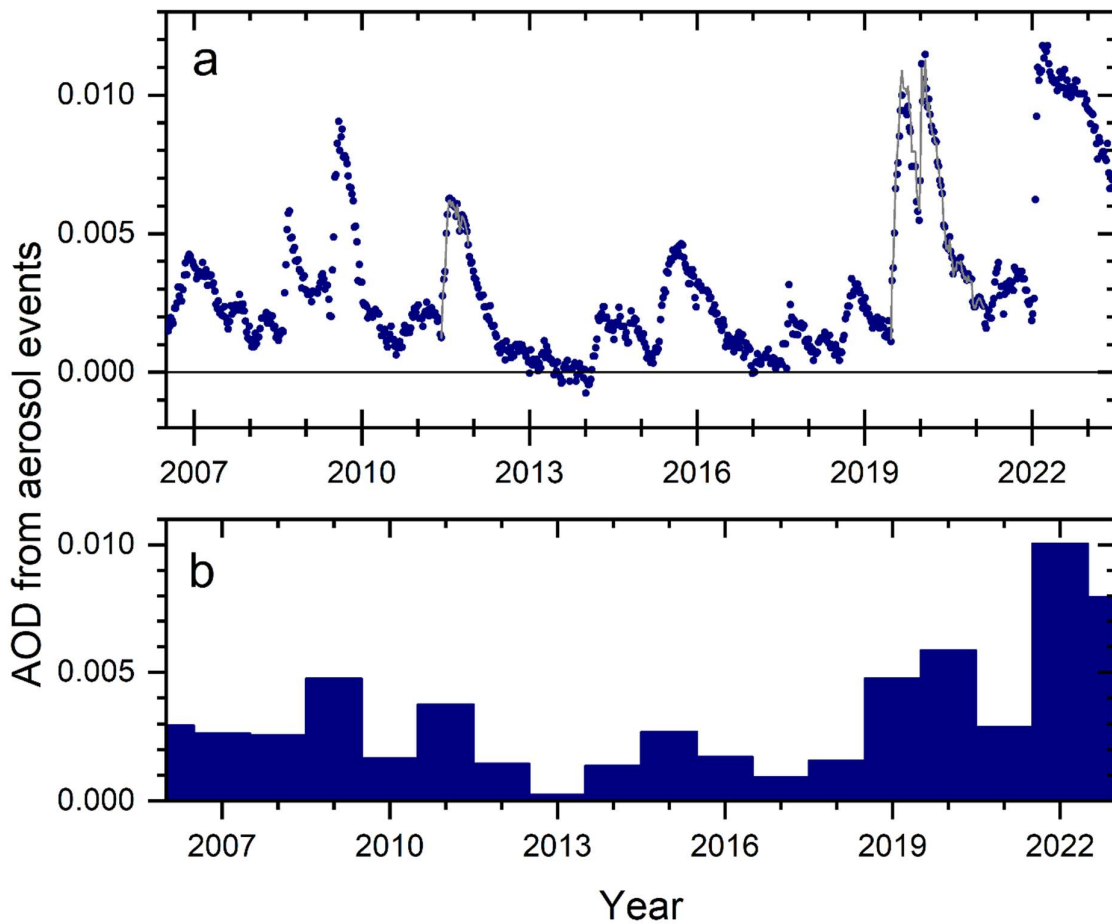
501 **3.4 Correction of lidar ratio**

502 Thus far we have presented AODs with the lidar ratio set to 50 sr. The lidar ratios of the
503 individual measurements are shown in Figure 2. In Figure 9a we show the averages with
504 statistical uncertainty (standard error and double-sided 95% confidence interval). As
505 already pointed out, three of the eruptions (Nabro 2011, Kelut 2014 and Soufriere 2021)
506 cannot be evaluated statistically due to few available measurements. Most of the
507 aerosol events show effective lidar ratios of approximately 50 sr, whereas the aerosol
508 from Puyehue-Cordón Caulle (2011), Raikoke (2019) and the Australian wildfires in the
509 end of 2019 deviates from 50 sr by more than 5%.

510 To convert the AOD obtained using $S_0 = 50$ sr to the estimated lidar ratio (S) we need to
511 consider the linear dependence of the AOD on the lidar ratio. A secondary effect relates
512 to the level of AOD. For the latter, we need to evaluate the occurrence of dense aerosol
513 layers. All the measurements fulfilling the criteria on uncertainty of the lidar ratio
514 estimate (Figure 1) are displayed in Figure 9b. Initially layer AODs sometimes exceed 1.
515 After 20 days the AOD of the individual aerosol layers is mostly 0.25 and lower, except
516 for the 2019 Australian wildfire that remain somewhat higher probably due to less air
517 mixing in the vortex formed (Kablick et al., 2020). We corrected the AODs by S/S_0 for
518 volcanic eruptions and wildfires that formed an aerosol with effective lidar ratio
519 deviating more than 5% from $S_0 = 50$ sr, whereas the residual correction connected with

520 the AOD of an aerosol layer was not accounted for (see the methods section for further
 521 detail) because the effect is small (Figure 9c). In the general evaluation we did not
 522 separate the aerosol backscattering from the 2019 and 2020 Australian wildfires that
 523 were only a few days apart. The 2020 fire was dominant in terms of AOD with 80 – 90%
 524 of the total AOD from the two fires (Friberg et al., 2023). Here, we weigh the lidar ratios
 525 of the two fires accordingly to obtain $S = 53.3$ representing both fires.

526



527

528 **Figure 10.** Background-subtracted AOD of the stratosphere from the tropopause to 35
 529 km altitude and averaged from -80 to 80° in latitude. a) AOD from main stratospheric
 530 aerosol events caused by volcanic eruptions and wildfires. AOD_{50} is shown (full grey
 531 line) where correction due to lidar ratio deviating from 50 sr is undertaken (Pu11, Ra19
 532 and Fi19&20). b) Yearly averages of data in a). Note that the horizontal tick marks
 533 indicate start of a year in a) and the middle of a year in b). Also note that the averages of
 534 years 2006 and 2023 span only half years due to the mid-year start (2006) and finish
 535 (2023) of the CALIOP measurements.

536

537 The blue dots in Figure 10a over the stratospheric AOD were corrected for deviant lidar
538 ratios in 2011 (Puyehue-Cordón Caulle eruption by +8%) and 2019 – 2020 (Raikoke
539 eruption by -12% and Australian wildfires by +7%). The corresponding AOD using $S_0 = 50$
540 sr is represented by a thin gray line showing that the AOD was practically not affected by
541 the correction in 2011 because that year was dominated by aerosol from another
542 eruption (Nabro, Figure 3). The AOD from the Raikoke (2019) eruption shifted down
543 slightly by the correction, and that of the 2019 – 2020 Australian wildfires shifted
544 upwards.

545 Altogether the changes in AOD from the corrections due to deviant lidar ratio were
546 found to be minor, the largest correction (-12%) was applied to the AOD of the Raikoke
547 eruption. However, we could not statistically quantify all major aerosol events, most
548 notably the Nabro eruption in 2011 (Figure 2). Our results show that assumption of an
549 effective lidar ratio of 50 sr works satisfactory in most cases in the 17-year period
550 studied when the stratospheric aerosol is influenced by volcanism or wildfires. The
551 applied method to obtain the effective lidar ratio cannot be used for optically thin layers
552 like the background aerosol.

553 **3.5 AOD of stratospheric aerosol events**

554 The AOD from aerosol events were approximately evenly distributed over the three
555 latitude regions (-80 to -20°, -20 to 20° and 20 to 80°) studied (Table 2). The altitude
556 distribution showed most influence from volcanic eruptions and wildfires in the sBD
557 (43%), followed by the dBD (31%), and the often overlooked LMS (Andersson et al.,
558 2015) held 26% of the AOD from aerosol events in the period 2006 – 2023.

559 The average stratospheric AOD, with the contribution from background aerosol
560 subtracted, from the tropopause to 35 km altitude in the latitude range -80 to 80° is
561 shown in Figure 10a. The intense volcanism – sea interaction of the Hunga Ha’apai
562 eruption in the beginning of 2022 (Martinsson et al., 2025) resulted in the highest and
563 broadest AOD peak (Figure 10a). Other prominent events were the Australian wildfires
564 at the end of 2019 and the beginning of 2020, the eruptions of Raikoke (2019), Sarychev
565 (2009), Nabro (2011), Calbuco (2015) and Kasatochi (2008) affecting the stratospheric

566 AOD together with several eruptions and wildfires having smaller contributions (Table
567 1).

568 The average influence of volcanic eruptions and wildfires each year is shown in Figure
569 10b. The most affected year was 2022 with an average AOD of 0.01 from aerosol events.
570 That year is likely followed by 2023, for which we have no data from the second half of
571 the year. Both these years were mainly affected by the 2022 Hunga Ha’apai eruption.
572 Then follows 2020 (mainly the 2019-20 Australian wildfires with some contribution from
573 the Raikoke eruption) with background-subtracted AOD of 0.006, 2009 (Sarychev) and
574 2019 (Raikoke) both years with AOD of 0.005, whereas 2011 (mainly Nabro) reach AOD
575 from aerosol events of almost 0.004. The average background-subtracted AOD from
576 volcanic eruptions and wildfires from 2006 to 2023 is 0.0031. The background aerosol
577 produces global average backscattering of 0.00011 sr^{-1} , which, with the commonly used
578 assumption of a lidar ratio of 50 sr, corresponds to a stratospheric background AOD of
579 0.0057.

580 The yearly average AOD from aerosol events ranges from 0.0002 (in 2013) to 0.010
581 (2022) and the average over the 17 years studied is 0.0031. Making use of previous
582 estimates of the relation between radiative forcing (F) and stratospheric AOD ($F = -$
583 $24 \times \text{AOD}$ in W/m^2) (Schmidt et al., 2018), we can obtain a first, simplified estimate of the
584 radiative effect of the stratospheric aerosol events. This relation is based on volcanic
585 sulfate aerosol, which is the dominant type of stratospheric aerosol event in the 17-year
586 period studied. The relation is not designed to deal with absorbing wildfire aerosol,
587 which cause uncertainty in the average radiative forcing of the period estimated here.
588 This simplified estimate of the global stratospheric yearly average total effective
589 radiative forcing due to volcanic eruptions and wildfires varies between -0.006 and -0.24
590 W/m^2 , with the average -0.074 W/m^2 in the period 2006 to 2023. Assuming a lidar ratio of
591 50 sr, the stratospheric background aerosol effective radiative forcing becomes -0.14
592 W/m^2 .

593 **4. Discussion**

594 Stratospheric aerosol optical properties are often described using solar occultation
595 data, especially from the 22 years of SAGE II measurements (Bauman et al., 2003;
596 Thomason et al., 2018). Prior comparisons of CALIOP lidar-based results with solar
597 occultation (SAGE III/ISS) show agreement within approximately 10% in the latitude
598 range -30 to 30° and increasing discrepancy at midlatitudes reaching above 50% at high
599 latitudes for background aerosol in the altitude range 20 – 30 km (Kar et al., 2019), and
600 discrepancies exceeding 50% is reported at altitudes below 17 km (Kovilakam et al.,
601 2023). The main reason for these differences was attributed to the unknown lidar ratio
602 of CALIOP (Kar et al., 2019; Kovilakam et al., 2023). Here we have estimated the CALIOP
603 effective lidar ratio of the aerosol from several volcanic eruptions and wildfires (Figure
604 2), and in Figure 9d the latitude distribution of the estimates is shown. Using the
605 standard lidar ratio of 50 sr cannot explain the latitude- and altitude-dependence in the
606 lidar – solar occultation comparison obtained in Kar et al. (2019) and Kovilakam et al.
607 (2023) for aerosol from volcanic eruptions and wildfires in the CALIOP era.

608 The latitude-dependent discrepancy at 532 nm wavelength between SAGE III/ISS and
609 CALIOP at high altitudes in the period June 2017 to August 2018 above 20 km (, i.e.,
610 essentially in the dBD) reported by Kar et al. (2019) concerns a period when the dBD
611 was close to background (Figure 7). The method used here for estimating the lidar ratio
612 does not work for background conditions (Figure 1). Using the standard CALIOP lidar
613 ratio for the background aerosol (50 sr) results in the global average background AOD of
614 0.0057. SAGE II measurements during the volcanically quiescent period 1998 – 2000
615 resulted in AOD of 0.0040 (estimated from Solomon et al. (2011), their Figure 2), who
616 integrated the stratospheric AOD from 15 km altitude. When removing the stratospheric
617 aerosol data below 15 km from the CALIOP measurements, the stratospheric
618 background AOD is reduced by 31% to 0.0039 using lidar ratio 50 sr. This is almost
619 identical to the background AOD reported in Solomon et al. (2011), thus indicating that
620 the stratospheric background aerosol on average has a lidar ratio close to 50 sr. Kar et
621 al. (2019) found that aerosol backscattering during background conditions at altitudes
622 above 20 km in the extratropics should be converted to AOD by a variable lidar ratio.
623 Mid- and high-latitude air in this altitude range has a high stratospheric age (~5 years)
624 (Ploeger et al., 2021), implying that particle gravitational settling has long time to affect

625 the particle size distribution, and hence the optical properties of the aerosol. In Figure
626 8c we find most of the aerosol above 20 km altitude to be located in the tropics,
627 implying that the deviations at high latitudes that Kar et al. (2019) reported have little
628 impact on global AOD, and thus little impact on our comparison with Solomon et al.
629 (2011) that deals with the entire stratosphere above 15 km altitude.

630 In a comparison by Kovilakam et al. (2023) between CALIOP and SAGE III/ISS during
631 November 2017, 2 – 3 months after the Canada/USA fire (Table 1) large deviations were
632 found at high latitudes and altitudes as in Kar et al. (2019), as described above.
633 Kovilakam et al. (2023) also found large differences in the densest part of the
634 stratosphere, i.e., at altitudes below 17 km. In GloSSAC the more than 50% lower values
635 of limb-viewing techniques (SAGE and OSIRIS) than CALIOP were adopted, justified by
636 citing uncertainties in the lidar ratio to discard CALIOP results at low altitudes
637 (Kovilakam et al., 2023).

638 The main advantages of solar occultation measurements are that extinction is
639 measured and that several wavelengths are available. Lidar measurements also have
640 some distinct advantages. Lidars with nadir view have several hundred kilometers
641 shorter measurement path enabling measurements in dense aerosol layers (Martinsson
642 et al., 2022, their Figure 7) producing viable, quantitative results when limb views fail,
643 provided that the lidar ratio is known. The lidar vertical resolution is superior and is not
644 relying on assumptions on homogeneity of the aerosol layer measured, like solar
645 occultation measurements do (Damadeo et al., 2013). Accurate altitude descriptions
646 with high vertical resolution of stratospheric injections (Sandvik et al., 2021) are vital for
647 the outcome of stratospheric aerosol modeling (Axebrink et al., 2025). Relying on these
648 points we argue that the role of lidar measurements should be re-evaluated. Existing
649 methods differ in their sensitivity to aerosol properties and in their temporal coverage.
650 We need to take advantage of the best qualities of all available methods, both in terms
651 of physical properties and time coverage. Re-evaluation of CALIOP data could improve
652 stratospheric aerosol climatologies, like GloSSAC (Thomason et al., 2018, Kovilakam et
653 al., 2020; Kovilakam et al., 2023), that are designed for the modeling community,
654 ultimately leading to a better representation of the stratospheric aerosol in climate
655 modeling.

656 Hopefully the lidar ratio of stratospheric aerosol can be further clarified when the
657 aerosol load is close to background conditions by lidar systems measuring both
658 backscattering and extinction. The ATLID aboard the EarthCARE satellite (Illingworth et
659 al., 2015) that started to produce data in July 2024 and the NASA and Italian Space
660 Agency collaboration on the 3 wavelength lidar CALIGOLA planned for launch in the
661 early 2030s (Behrenfeld et al., 2023) are future means to further clarify extinction
662 obtained from lidars, and to optimally combine solar occultation and lidar
663 measurements for future long-term records on the optical properties of the
664 stratospheric aerosol with high and unambiguous vertical resolution.

665 **5. Conclusions**

666 The entire backscattering record at 532 nm wavelength of the satellite-based lidar
667 system CALIOP spanning years 2006 to 2023 was investigated in this study. During this
668 period injections of aerosol and precursor gases into the stratosphere of 15 volcanic
669 eruptions and 5 wildfires were identified. The effective lidar ratios of 12 volcanic
670 eruptions and wildfires were investigated to convert the measured backscattering to
671 extinction. The measurements were evaluated and corrected for attenuation using the
672 lidar ratio $S_0 = 50$ sr. The aerosol events having a lidar ratio deviating by more than 5%
673 from S_0 were corrected after the general evaluation.

674 Background aerosol conditions are more likely to occur in sublayers than throughout
675 the entire stratosphere. The stratosphere was therefore subdivided into 9 layers
676 spanned by altitude (lowermost stratosphere (LMS), shallow Brewer-Dobson branch
677 (sBD), deep Brewer-Dobson branch (dBD)) and latitude intervals (tropics and Southern
678 and Northern extratropics). The backgrounds of layers were combined to obtain the
679 background aerosol of the entire stratosphere. The backscattering of background
680 aerosol was converted to aerosol optical depth (AOD) using a lidar ratio of 50 sr. That
681 AOD agrees well with measurements with solar occultation (SAGE II) during 1998 – 2000
682 in the volcanically quiescent period. The average backscattering of seven of the nine
683 layers each contains 11 - 15% of the entire background aerosol. The tropical LMS has a
684 small contribution due to very small volume compared to the other layers. The tropical
685 sBD was also clearly lower (7%) because oxidation of carbonyl sulfide (OCS) occurs at

686 higher altitudes in the upwards moving air in the tropical stratosphere. We find that 70%
687 of the aerosol in the tropical dBD is formed above 19 km altitude during background
688 conditions, due to formation from OCS. A several kilometers thick band of low aerosol
689 load directly above the tropopause was identified which we attribute to young
690 stratospheric air transported in the sBD. Above that layer a broad band with high aerosol
691 load was found which we identify as the tropical dBD air that after poleward followed by
692 downward transport to the sBD and LMS results in high aerosol load at mid and high
693 latitudes. Considering the ongoing debate on the sources of stratospheric background
694 aerosol, these highly resolved CALIOP data could be useful to constrain modeling
695 efforts on the sources of the stratospheric sulfurous aerosol.

696 The background aerosol AOD (0.0057) was subtracted from the measurements to
697 obtain the influence from aerosol and trace gas injections into the stratosphere. The
698 most important aerosol events in the 17-year period are the 2022 Hunga Ha'apai
699 eruption and the Australian wildfires (2019-20) followed by the volcanic eruptions
700 Raikoke (2019), Sarychev (2009) and Nabro (2011). The global yearly average AOD
701 increase from volcanic and wildfire injections spans 0 to 0.010.

702 Limb-viewing solar occultation measurements have some distinctive advantages in that
703 much of the early measurements in the satellite era were undertaken with that method.
704 They also deliver direct measurements of extinction, and at several wavelengths. Here,
705 we have estimated the effective lidar ratio of the CALIOP measurements to obtain
706 extinction from backscattering measurements. Lidars operating in nadir view, like
707 CALIOP, have several hundred kilometers (or a factor of more than 100) shorter
708 measurement path than limb-viewers, allowing measurements in dense aerosol layers
709 where limb-viewers fail. Lidars have unambiguous and superior vertical resolution over
710 other satellite instruments providing models with important input on aerosol and trace
711 gas injections into the stratosphere. Newer lidars that measure extinction are launched,
712 under construction and planned. Now is the time to better sort out differences between
713 lidars and solar occultation measurements. With known effective lidar ratios the
714 relation between CALIOP and solar occultation measurements need to be re-evaluated,
715 especially in the dense stratospheric air located below 17 km altitude in long-term
716 records over the optical properties of the stratospheric aerosol.

717 **References**

- 718 Andersson, S. M., Martinsson, B. G., Friberg, J., Brenninkmeijer, C. A. M., Rauthe-
719 Schöch, A., Hermann, M., van Velthoven, P. F. J., and Zahn, A.: Composition and
720 evolution of volcanic aerosol from eruptions of Kasatochi, Sarychev and
721 Eyjafjallajökull in 2008–2010 based on CARIBIC observations, *Atmos. Chem.*
722 *Phys.*, 13, 1781–1796, <https://doi.org/10.5194/acp-13-1781-2013>, 2013.
- 723 Andersson, S. M., Martinsson, B. G., Vernier, J.-P., Friberg, J., Brenninkmeijer, C. A. M.,
724 Hermann, M., van Velthoven, P. F. J., and Zahn, A.: Significant radiative impact of
725 volcanic aerosol in the lowermost stratosphere, *Nat. Commun.*, 6, 1–8,
726 <https://doi.org/10.1038/ncomms8692>, 2015.
- 727 Appenzeller, C., Holton, J.R., and Rosenlov, K.H.: Seasonal variation of mass transport
728 across the tropopause, *J. Geophys. Res.* 101, 15071-15078, 1996.
- 729 Austin, J., and Li, F.: On the relationship between the strength of the Brewer-Dobson
730 circulation and the age of stratospheric air, *Geophys. Res. Lett.*, 33, L17807,
731 [doi:10.1029/2006GL026867](https://doi.org/10.1029/2006GL026867), 2006.
- 732 Axebrink, E., Sporre, M.K., and Friberg, J.: Impact of SO₂ injection profiles on simulated
733 volcanic forcing for the 2009 Sarychev eruptions– investigating the importance of
734 using high-vertical-resolution methods when compiling SO₂ data, *Atmos. Chem.*
735 *Phys.*, 25, 2047–2059, <https://doi.org/10.5194/acp-25-2047-2025>, 2025.
- 736 Bauman, J. J., Russell, P. B., Geller, M. A., and Hamill, P.: A stratospheric aerosol
737 climatology from SAGE II and CLAES measurements: 2. Results and
738 comparisons, 1984–1999, *J. Geophys. Res.*, 108, 4383,
739 <https://doi.org/10.1029/2002JD002993>, 2003.
- 740 Behrenfeld, M.J., Lorenzoni, L., Hu, Y., Bissom, K.M., Hostetler, C.A., Di Girolamo, P.,
741 Dionisi, D., Longo, F., and Zoffoli, S.: Satellite Lidar Measurements as a Critical
742 New Global Ocean Climate Record, *Remote Sens.* 15, 5567. [https://doi.org/](https://doi.org/10.3390/rs15235567)
743 [10.3390/rs15235567](https://doi.org/10.3390/rs15235567), 2023.
- 744 Brühl, C., Lelieveld, J., Crutzen, P.J., and Tost, H.: The role of carbonyl sulphide as a
745 source of stratospheric sulphate aerosol and its impact on climate, *Atmos.*
746 *Chem. Phys.*, 12, 1239–1253, www.atmos-chem-phys.net/12/1239/2012/
747 [doi:10.5194/acp-12-1239-2012](https://doi.org/10.5194/acp-12-1239-2012), 2012.
- 748 Butchart, N., The Brewer-Dobson circulation, *Rev. Geophys.*, 52, 157–184,
749 [doi:10.1002/2013RG000448](https://doi.org/10.1002/2013RG000448), 2014.
- 750 Carn, S.A., Krueger, A.J., Krotkov, N.A., Yang, K., and Evans, K.: Tracking volcanic sulfur
751 dioxide clouds for aviation hazard mitigation, *Nat Hazards*, 51, 325–343 DOI
752 [10.1007/s11069-008-9228-4](https://doi.org/10.1007/s11069-008-9228-4), 2009.

- 753 Carn, S.A., and Prata, F.J., Satellite-based constraints on explosive SO₂ release from
754 Soufrière Hills Volcano, Montserrat, *Geophys. Res. Lett.*, 37, 1-5, L00E22,
755 doi:10.1029/2010GL044971, 2010.
- 756 Carn, S. A., Krotkov, N. A., Fisher, B. L., and Li, C.: Out of the blue: Volcanic SO₂
757 emissions during the 2021–2022 eruptions of Hunga Tonga– Hunga Ha’apai
758 (Tonga), *Front. Earth Sci.*, 10, 976962,
759 <https://doi.org/10.3389/feart.2022.976962>, 2022.
- 760 Chin, M., and Davies, D.D.: A reanalysis of carbonyl sulfide as a source of stratospheric
761 background sulfur aerosol, *J. Geophys. Res.* 100, 8993-9005, 1995.
- 762 Clarisse, L., Hurtmans, D., Clerbaux, C., Hadji-Lazaro, J., Ngadi, Y., and Coheur, P.-F.:
763 Retrieval of sulphur dioxide from the infrared atmospheric sounding
764 interferometer (IASI), *Atmos. Meas. Tech.*, 5, 581–594,
765 <https://doi.org/10.5194/amt-5-581> 2012, 2012.
- 766 Clarisse, L., Coheur, P.-F., Prata F., Hadji-Lazaro, J., Hurtmans, D., and Clerbaux, C.: A
767 unified approach to infrared aerosol remote sensing and type specification,
768 *Atmos.Chem.Phys.*, 13, 2195–2221, www.atmos-chem-phys.net/13/2195/2013/
769 doi:10.5194/acp-13-2195-2013, 2013.
- 770 Crutzen, P.J.: The possible importance of CSO for the sulfate layer of the stratosphere,
771 *Geophys. Res. Lett.* 3, 73-76, 1976.
- 772 Cruz, M.G., Sullivan, A.L., Gould, J.S., Sims, N.C., Bannister, A.J., Hollis, J.J., and Hurley,
773 R.J.: Anatomy of a catastrophic wildfire: The Black Saturday Kilmore East fire in
774 Victoria, Australia, *Forest Ecol. Manag.* 284, 269-295, 2012.
- 775 Damadeo, R.P., Zawodny, J.M., Thomason, L.W., and Iyer, N.: SAGE version 7.0
776 algorithm: application to SAGE II, *Atmos. Meas. Tech.*, 6, 3539–3561,
777 www.atmos-meas-tech.net/6/3539/2013/, 2013.
- 778 Friberg, J., Martinsson, B. G., Andersson, S. M., Brenninkmeijer, C. A. M., Hermann, M.,
779 Van Velthoven, P. F. J., and Zahn, A.: Sources of increase in lowermost
780 stratospheric sulphurous and carbonaceous aerosol background concentrations
781 during 1999–2008 derived from CARIBIC flights, *Tellus B*, 66, 23428,
782 <https://doi.org/10.3402/tellusb.v66.23428>, 2014.
- 783 Friberg, J., Martinsson, B. G., Andersson, S. M., and Sandvik, O. S.: Volcanic impact on
784 the climate– the stratospheric aerosol load in the period 2006–2015, *Atmos.*
785 *Chem. Phys.*, 18, 11149–11169, <https://doi.org/10.5194/acp-18-11149-2018>,
786 2018.
- 787 Friberg, J., Martinsson, B. G., and Sporre, M. K.: Short- and long-term stratospheric
788 impact of smoke from the 2019–2020 Australian wildfires, *Atmos. Chem. Phys.*,
789 23, 12557–12570, <https://doi.org/10.5194/acp-23-12557-2023>, 2023.

- 790 Fromm, M., Lindsey, D. T., Servranckx, R., Yue, G., Trickl, T., Sica, R., Doucet, P., and
791 Godin-Beekmann, S.: The untold story of pyrocumulonimbus, *B. Am. Meteorol.*
792 *Soc.*, 91, 1193–1209, 2010.
- 793 Fromm, M., Kablick III, G. P., Peterson, D. A., Kahn, R. A., Flower, V. J. B., and Seftor, C. J.:
794 Quantifying the source term and uniqueness of the August 12, 2017 Pacific
795 Northwest pyroCb event, *J. Geophys. Res.*, 126, e2021JD034928,
796 <https://doi.org/10.1029/2021JD034928>, 2021.
- 797 Garofalo, L. A., Levin, E. J. T., Campos, T., Kreidenweis, S. N., and Farmer, D. K.:
798 Emission and evolution of submicron organic aerosol in smoke from wild fires in
799 the western United States, *ACS Space Chem.*, 3, 1237–1247, 2019.
- 800 Gelaro, R., McCarty, W., Suarez, M. J., Todling, R., Moloud, A., Takacs, L., Randles, C. A.,
801 Darmenov, A., Bosilovich, M. G., Reichle, R., Wargan, K., Coy, L., Cullather, R.,
802 Draper, C., Akella, S., Buchard, V., Conaty, A., da Silva, A. M., Gu, W., Kim, G.-K.,
803 Koster, R., Lucchesi, R., Merkova, D., Nielsen, J. E., Partyka, G., Pawson, S.,
804 Putman, W., Rienecker, M., Schubert, S. D., Seinkiewicz, M., and Zhao, B.: The
805 Modern-Era Retrospective Analysis for Research and Applications, Version 2
806 (MERRA-2), *J. Clim.* 30, 5419-5454, 2017.
- 807 Haywood, J.M., Jones, A., Clarisse, L., Bourassa, A., Barnes, J., Telford, P., Bellouin, N.,
808 Boucher, O., Agnew, P., Clerbaux, C., Coheur, P., Degenstein, D., and Braesicke,
809 P.: Observations of the eruption of the Sarychev volcano and simulations using
810 the HadGEM2 climate model, *J. Geophys. Res.*, 115, D21212,
811 [doi:10.1029/2010JD014447](https://doi.org/10.1029/2010JD014447), 2010.
- 812 Illingworth, A. J., Barker, H. W., Beljaars, A., Ceccaldi, M., Chepfer, H., Clerbaux, N.,
813 Cole, J., Delanoë, J., Domenech, C., Donovan, D. P., Fukuda, S., Hirakata, M.,
814 Hogan, R. J., Huenerbein, A., Kollias, P., Kubota, T., Nakajima, T., Nakajima, T. Y.,
815 Nishizawa, T., Ohno, Y., Okamoto, H., Oki, R., Sato, K., Satoh, M., Shephard, M.
816 W., Velázquez-Blázquez, A., Wandinger, U., Wehr, T., and van Zadelhoff, G.-J.: The
817 Earth CARE Satellite: The Next Step Forward in Global Measurements of Clouds,
818 Aerosols, Precipitation, and Radiation, *B. Am. Meteorol. Soc.*, 96, 1311–1332,
819 <https://doi.org/10.1175/BAMS-D-12-00227.1>, 2015.
- 820 Junge, C.E., Chagnon, C.W., and Manson, J.E.: A World-wide Stratospheric Aerosol
821 Layer, *Science*, 133, 1478-1479, 1961.
- 822 Kablick, G. P., Allen, D. R., Fromm, M. D., and Nedoluha, G. E.: Australian PyroCb Smoke
823 Generates Synoptic-Scale Stratospheric Anticyclones, *Geophys. Res. Lett.*, 47,
824 e2020GL08810, <https://doi.org/10.1029/2020GL088101>, 2020.
- 825 Kar, J., Lee, K.-P., Vaughan, M. A., Tackett, J. L., Trepte, C. R., Winker, D. M., Lucker, P. L.,
826 and Getzewich, B. J.: CALIPSO level 3 stratospheric aerosol profile product:
827 version 1.00 algorithm description and initial assessment, *Atmos. Meas. Tech.*,
828 12, 6173–6191, <https://doi.org/10.5194/amt-12-6173-2019>, 2019.

- 829 Kloss, C., Berthet, G., Sellitto, P., Ploeger, F., Taha, G., Tidiga, M., Eremanko, M.,
830 Bossolasco, A., Jégou, F., Renard, J.-B., and Legras, B.: Stratospheric aerosol
831 layer perturbation caused by the 2019 Raikoke and Ulawun eruptions and their
832 radiative forcing, *Atmos. Chem. Phys.*, 21, 535–560, <https://doi.org/10.5194/acp-21-535-2021>, 2021.
- 834 Kovilakam, M., Thomason, L.W., Ernest, N., Rieger, L.A., Bourassa, A.E., and Millán, L.:
835 The Global Space-based Stratospheric Aerosol Climatology (version 2.0): 1979–
836 2018, *Earth Syst. Sci. Data*, 12, 2607–2634, <https://doi.org/10.5194/essd-12-2607-2020>, 2020.
- 838 Kovilakam, M., Thomason, L.W., and Knepp, T.: SAGEIII/ISS aerosol/cloud categorization
839 and its impact on GloSSAC, *Atmos. Meas. Tech.*, 16, 2709–2731,
840 <https://doi.org/10.5194/amt-16-2709-2023>, 2023.
- 841 Kremser, S., Thomason, L. W., von Hobe, M., Hermann, M., Desher, T., Timmreck, C.,
842 Toohey, M., Stenke, A., Schwarz, J. P., Weigel, R., Fueglistaler, S., Prata, F. J.,
843 Vernier, J. P., Schlager, H., Barnes, J. E., Antuña-Marrero, J. C., Fairlie, D., Palm,
844 M., Mahieu, E., Notholt, J., Rex, M., Bingen, C., Vanhellefont, F., Bourassa, A.,
845 Plane, J. M. C., Klocke, D., Carn, S. A., Clarisse, L., Trickl, T., Neely, R., James, A.
846 D., Rieger, L., Wilson, J. C., and Meland, B.: Stratospheric aerosol– Observations,
847 processes, and impact on climate, *Rev. Geophys.*, 54, 278–335,
848 <https://doi.org/10.1002/2015RG000511>, 2016.
- 849 Li, C., Krotkov, N.A., Carn, S., Zhang, Y., Spurr, R.D.J., and Joiner, J.: New-generation
850 NASA Aura Ozone Monitoring Instrument (OMI) volcanic SO₂ dataset: algorithm
851 description, initial results, and continuation with the Suomi-NPP Ozone Mapping
852 and Profiler Suite (OMPS), *Atmos. Meas. Tech.*, 10, 445–458, www.atmos-meas-tech.net/10/445/2017/, doi:10.5194/amt-10-445-2017, 2017.
- 854 Lin, P., and Fu, Q., Changes in various branches of the Brewer–Dobson circulation from
855 an ensemble of chemistry climate models, *J. Geophys. Res.*, 118, 73–84,
856 doi:10.1029/2012JD018813, 2013.
- 857 Malinina, E., Rozanov, A., Niemayer, U., Wallis, S., Arosio, C., Wrana, F., Timmreck, C.,
858 von Savigny, C., and Burrows, J.P.: Changes in stratospheric aerosol extinction
859 coefficient after the 2018 Ambae eruption as seen by OMPS-LP and MAECHAM5-
860 HAM, *Atmos. Chem. Phys.*, 21, 14871–14891, <https://doi.org/10.5194/acp-21-14871-2021>, 2021.
- 862 Martinsson, B. G., Nguyen, H. N., Brenninkmeijer, C. A. M., Zahn, A., Heintzenberg, J.,
863 Hermann, M., and Velthoven, P. F. J. v.: Characteristics and origin of lowermost
864 stratospheric aerosol at northern midlatitudes under volcanically quiescent
865 conditions based on CARIBIC observations, *J. Geophys. Res.*, 110, D12201,
866 doi:10.1029/2004JD005644, 2005.
- 867 Martinsson, B. G., Brenninkmeijer, C. A. M., Carn, S. A., Hermann, M., Heue, K.P., van
868 Velthoven, P. F. J., and Zahn, A.: Influence of the 2008 Kasatochi volcanic

869 eruption on sulfurous and carbonaceous aerosol constituents in the lower
870 stratosphere, *Geophys. Res. Lett.*, 36, 1–5,
871 <https://doi.org/10.1029/2009GL038735>, 2009.

872 Martinsson, B. G., Friberg, J., Sandvik, O. S., Hermann, M., van Velthoven, P. F. J., and
873 Zahn, A.: Particulate sulfur in the upper troposphere and lowermost
874 stratosphere– sources and climate forcing, *Atmos. Chem. Phys.*, 17, 10937–
875 10953, <https://doi.org/10.5194/acp-17-10937-2017>, 2017.

876 Martinsson, B. G., Friberg, J., Sandvik, O. S., Hermann, M., van Velthoven, P. F. J., and
877 Zahn, A.: Formation and composition of the UTLS aerosol, *npj Climate and
878 Atmospheric Science*, 2, 1–6, <https://doi.org/10.1038/s41612-019-0097-1>, 2019.

879 Martinsson, B. G., Friberg, J., Sandvik, O. S., and Sporre, M. K.: Five-satellite-sensor
880 study of the rapid decline of wildfire smoke in the stratosphere, *Atmos. Chem.
881 Phys.*, 22, 3967–3984, <https://doi.org/10.5194/acp-22-3967-2022>, 2022.

882 Martinsson, B. G., Friberg, J., and Sporre, M. K.: Stratospheric aerosol formed by intense
883 volcanism–sea interaction during the 2022 Hunga Ha’apai eruption, *Atmos.
884 Chem. Phys.*, 25, 10677–10690, <https://doi.org/10.5194/acp-25-10677-2025>,
885 2025.

886 Mastin, L. G., Van Eaton, A. R., and Cronin, S. J.: Did steam boost the height and growth
887 rate of the giant Hunga eruption plume?, *B. Volcanol.*, 86, 64,
888 <https://doi.org/10.1007/s00445-024-01749-1>, 2024.

889 McCarthy, G.J., Plucinski, M.P., and Gould, J.S.: Analysis of the resourcing and
890 containment of multiple remote fires: The Great Divide Complex of fires, Victoria,
891 December 2006, *Australian Forestry*, 75, 54-63, DOI:
892 10.1080/00049158.2012.10676385, 2012.

893 Mote, P.W., Dunkerton, T.J., McIntyre, M.E., Ray, E.A., Haynes, P.H., and Russell III, J.M.:
894 Vertical velocity, vertical diffusion, and dilution by midlatitude air in the tropical
895 lower stratosphere, *J. Geophys. Res.* 103, 8651-8666, 1998.

896 Murphy, D. M., Cziczo, D. J., Hudson, P. K., and Thomson, D. S.: Carbonaceous material
897 in aerosol particles in the lower stratosphere and tropopause region, *J. Geophys.
898 Res.*, 112, D04203, <https://doi.org/10.1029/2006JD007297>, 2007.

899 NASA/LARC/SD/ASDC: Science CALIPSO Lidar Level 1B profile data, V4-51, NASA
900 Langley Atmospheric Data Center DAAC,
901 https://doi.org/10.5067/CALIOP/CALIPSO/CAL_LID_L1 Standard-V4-51, 2024.

902 Nicknish, P.A., Stone, K., Solomon, S., and Carn, S.A.: Quantifying the decay timescale
903 of volcanic sulfur dioxide in the stratosphere, *Atmos. Chem. Phys.*, 25, 11535–
904 11555, <https://doi.org/10.5194/acp-25-11535-2025>, 2025.

905 Ohneiser, K., Ansmann, A., Baars, H., Seifert, P., Barja, B., Jimenez, C., Radenz, M.,
906 Tiesseire, A., Floutsi, A., Haarig, M., Foth, A., Chudnovsky, A., Engelmann, R.,

- 907 Zamorano, F., Bühl, J., and Wandinger, U.: Smoke of extreme Australian bushfires
 908 observed in the stratosphere over Punta Arenas, Chile, in January 2020: optical
 909 thickness, lidar ratios, and depolarization ratios at 355 and 532nm, *Atmos.*
 910 *Chem. Phys.*, 20, 8003–8015, <https://doi.org/10.5194/acp-20-8003-2020>, 2020.
- 911 Pardini, F., Burton, M., Arzilli, F., La Spina, G., and Polacci, M.: SO₂ emissions, plume
 912 heights and magmatic processes inferred from satellite data: The 2015 Calbuco
 913 eruptions, *J. Volcanol. Geotherm. Res.* 361, 12-24, 2018.
- 914 Peterson, D. A., Fromm, M. D., McRae, R. H. D., Campbell, J. R., Hyer, E. J., Taha, G.,
 915 Camacho, C. P., Kablick, G. P., Schmidt, C. C., and DeLand, M. T.: Australia's
 916 Black Summer pyrocumulonimbus super outbreak reveals potential for
 917 increasingly extreme stratospheric smoke events, *Npj Clim. Atmos. Sci.*, 4, 38
 918 <https://doi.org/10.1038/s41612-021-00192-9>, 2021.
- 919 Peterson, D. A., Berman, M. T., Fromm, M. D., Servranckx, R., Julstrom, W. J., Hyer, E. J.,
 920 Campbell, J. R., McHardy, T. M., and Lambert, A.: Worldwide inventory reveals
 921 the frequency and variability of pyrocumulonimbus and stratospheric smoke
 922 plumes during 2013–2023, *Npj Clim. Atmos. Sci.*, 8, 325,
 923 <https://doi.org/10.1038/s41612-025-01188-5>, 2025.
- 924 Ploeger, F., Diallo, M., Charlesworth, E., Konopka, P., Legras, B., Laube, J.C., Gross, J.-U.,
 925 Günther, G., Engel, A., and Riese, M.: The stratospheric Brewer–Dobson
 926 circulation inferred from age of air in the ERA5 reanalysis, *Atmos. Chem. Phys.*,
 927 21, 8393–8412, <https://doi.org/10.5194/acp-21-8393-2021>, 2021.
- 928 Prata, A. T., Young, S. A., Siems, S. T., and Manton, M. J.: Lidar ratios of stratospheric
 929 volcanic ash and sulfate aerosols retrieved from CALIOP measurements, *Atmos.*
 930 *Chem. Phys.*, 17, 8599–8618, <https://doi.org/10.5194/acp-17-8599-2017>, 2017.
- 931 Rieger, L.A., Bourassa, A.E., and Degenstein, D.A.: Merging the OSIRIS and SAGE II
 932 stratospheric aerosol records, *J. Geophys. Res. Atmos.*, 120, 8890–8904,
 933 doi:10.1002/2015JD023133, 2015.
- 934 Sandvik, O. S., Friberg, J., Sporre, M. K., and Martinsson, B. G.: Methodology to obtain
 935 highly resolved SO₂ vertical profiles for representation of volcanic emissions in
 936 climate models, *Atmos. Meas. Tech.*, 14, 7153–7165,
 937 <https://doi.org/10.5194/amt-14-7153-2021>, 2021.
- 938 Sato, M., Hansen, J.E., McCormick, M.P., and Pollack J.B.: Stratospheric aerosol optical
 939 depths, 1850-1990, *J. Geophys. Res.* 98, 22987-22994, 1993.
- 940 Schmidt, A., Mills, M. J., Ghan, S., Gregory, J. M., Allan, R. P., Andrews, T., Bardeen, C. G.,
 941 Conley, A., Forster, P. M., Gettelman, A., Portmann, R. W., Solomon, S., and Toon,
 942 O. B.: Volcanic radiative forcing from 1979 to 2015, *J. Geophys. Res.-Atmos.*, 123,
 943 12491–12508, <https://doi.org/10.1029/2018JD028776>, 2018.
- 944 Seabrook, S., Mackay, K., Watson, S. J., Clare, M. A., Hunt, J. E., Yeo, I. A., Lane, E. M.,
 945 Clark, M. R., Wysoczanski, R., Rowden, A.A., Kula, T., Hoffmann, L.J., Armstrong,

946 E., and Williams, M. J. M.: Volcaniclastic density currents explain widespread
947 and diverse seafloor impacts of the 2022 Hunga Volcano eruption, *Nat.*
948 *Commun.*, 14, 7881, <https://doi.org/10.1038/s41467-023-43607-2>, 2023.

949 Sheng, J.-X., Weisenstein, D.K., Luo, B.-P., Rozanov, E., Stenke, A., Anet, J., Bingemer, H.,
950 and Peter, T.: Global atmospheric sulfur budget under volcanically quiescent
951 conditions: Aerosol-chemistry-climate model predictions and validation, *J.*
952 *Geophys. Res. Atmos.*, 120, 256–276, doi:10.1002/2014JD021985, 2015.

953 Solomon, S., Daniel, J. S., Neely, R. R., Vernier, J.-P., Dutton, E. G., and Thomason, L. W.:
954 The persistently variable “background” stratospheric aerosol layer and global
955 climate change, *Science*, 333, 866–870, 2011.

956 Surano, Jousset, P., Pallister, J., Boichu, M., Boungiorno, M.F., Budisantoso, A., Costa, F.,
957 Andreastuti, S., Prata, F., Schneider, D., Clarisse, L., Humaida, H., Sumarti, S.,
958 Bignami, C., Griswold, J., Carn, S., Oppenheimer C., and Lavigne F.: The 2010
959 explosive eruption of Java's Merapi volcano—A ‘100-year’ event, *J. Volcanol.*
960 *Geotherm. Res.* 241-242, 121-135, 2012.

961 Taylor, I. A., Grainger, R. G., Prata, A. T., Proud, S. R., Mather, T. A., and Pyle, D. M.: A
962 satellite chronology of plumes from the April 2021 eruption of La Soufrière, St
963 Vincent, *Atmos. Chem. Phys.*, 23, 15209–15234, [https://doi.org/10.5194/acp-23-](https://doi.org/10.5194/acp-23-15209-2023)
964 [15209-2023](https://doi.org/10.5194/acp-23-15209-2023), 2023.

965 Thomas, H.E., Watson, I.M., Carn, S.A., Prata, A.J., and Realmuta, V.J.: A comparison of
966 AIRS, MODIS and OMI sulphur dioxide retrievals in volcanic clouds, *Geomatics,*
967 *Natural Hazards and Risk*, 2, 217-232, 2011.

968 Thomason, L.W., Ernest, N., Millán, L., Rieger, L., Bourassa, A., Vernier, J.-P., Manney, G.,
969 Luo, B., Arfeuille, F., and Peter, T.: A global space-based stratospheric aerosol
970 climatology: 1979-2016, *Earth Syst. Sci. Data*, 10, 469–492,
971 <https://doi.org/10.5194/essd-10-469-2018>, 2018.

972 Vernier, J.-P., Pommereau, J.P., Garnier, A., Pelon, J., Larsen, N., Nielsen, J.,
973 Christiansen, T., Cairo, F., Thomason, L.W., Leblanc, T., and McDermid, I.S.:
974 Tropical stratospheric aerosol layer from CALIPSO lidar observations, *J.*
975 *Geophys. Res.*, 114, D00H10, doi:10.1029/2009JD011946, 2009.

976 Vernier, J.-P., Farlie, T.D., Murray, J.J., Tupper, A., Trepte, C., Winker, D., Pelon, J., Garnier,
977 A., Jumelet, J., Pavolonis, M., Omar, A.H., and Powell, K.A.: An Advanced System
978 to Monitor the 3D Structure of Diffuse Volcanic Ash Clouds *J. Appl. Meteorol.*
979 *Clim.* 10, 2125-2138, 2013.

980 Vernier, J.-P., Farlie, T.D., Natarajan, M., Wiengold, F.G., Bian, J., Martinsson, B.G.,
981 Crumeyrolle, S., Thomason, L.W., and Bedka, K.M.: Increase in upper
982 tropospheric and lower stratospheric aerosol levels and its potential connection
983 with Asian pollution, *J. Geophys. Res.*, 120, doi:10.1002/2014JD022372, 2015.

984 Weisenstein, D.K., Yue, G.K., Ko, M.K.W., Sze, N.-D., Rodriguez, J.M., and Scott, C.J.: A
985 two-dimensional model of sulfur species and aerosol, *J. Geophys. Res.* 102,
986 13019-13035, 1997.

987 Winker, D. M., Hunt, W. H., and McGill, M. J.: Initial performance assessment of CALIOP,
988 *Geophys. Res. Lett.*, 34, 1–5, <https://doi.org/10.1029/2007GL030135>, 2007.

989 Winker, D. M., Pelon, J., Coakley, J. A., Ackerman, S. A., Charlson, R. J., Colarco, P. R.,
990 Flamant, P., Fu, Q., Hoff, R. M., Kittaka, C., Kubar, T. L., Le Treut, H., McCormick,
991 M. P., Mégie, G., Poole, L., Powell, K., Trepte, K., Vaughan, M. A., and Wielicki, B.
992 A.: The CALIPSO mission– A global 3D view of aerosols and clouds, *B. Am.*
993 *Meteorol. Soc.*, 91, 1211–1229, <https://doi.org/10.1175/2010BAMS3009.1>, 2010.

994 *Data availability.* The data used are publicly available: CALIOP V4.51 lidar data
995 (<https://search.earthdata.nasa.gov/search?fp=CALIPSO>).

996 *Author contributions.* BGM planned the study, undertook most of the data analysis and
997 wrote the paper. JF participated in the planning of the study, undertook part of the data
998 analysis and MKS contributed. JF and MKS undertook data extraction and handling for
999 the data analysis. All authors participated in discussions and commented on the
1000 manuscript.

1001 *Disclaimer.* The contact author and the co-authors declare that they have no competing
1002 interests.

1003 *Acknowledgements.* Aerosol products from the CALIOP sensor were produced by NASA
1004 Langley Research Center.

1005 *Financial support.* The Swedish National Space Agency, contracts 2025-00200 and
1006 2022-00157, Johan Friberg. The Crafoord Foundation, contract 20240901, Johan Friberg.
1007 Formas, contract 2025-01869, Johan Friberg. Formas, contract 2020-00997, Moa
1008 Sporre. The Swedish Research Council 2022-02836, Moa Sporre.